

# 1 A top-down evaluation of bottom-up estimates to reduce uncertainty 2 in methane emissions from Arctic wetlands

3  
4 Luana S. Basso<sup>1</sup>, Goran Georgievski<sup>2,3</sup>, Victor Brovkin<sup>2</sup>, Christian Beer<sup>4,5</sup>, Christian Rödenbeck<sup>1</sup>, Mathias  
5 Göckede<sup>1</sup>

6 <sup>1</sup>Department of Biogeochemical Signals, Max Planck Institute for Biogeochemistry, Jena, 07745, Germany

7 <sup>2</sup>Department of Climate Dynamics, Max Planck Institute for Meteorology, Hamburg, 20146, Germany

8 <sup>3</sup>[Earth Resilience Science Unit, Potsdam Institute for Climate Impact Research, Germany](#)

9 <sup>4,5</sup>Department of Earth System Sciences, University of Hamburg, Hamburg, 20146, Germany

10 *Correspondence to:* Luana S. Basso (lbasso@bgc-jena.mpg.de)

## 11 Abstract.

12 Wetlands are a major natural source of atmospheric CH<sub>4</sub>, however, accurately estimating their emissions is difficult due  
13 to the complex biogeochemical interactions and spatial heterogeneity of wetland environments. This study explores how a  
14 combination of atmospheric inverse and process-based modelling can reduce the discrepancy in Arctic wetland estimates  
15 between bottom-up and top-down approaches. We employed the Jena CarboScope global inversion system, incorporating prior  
16 wetland fluxes simulated by the JSBACH land surface model, which is part of the Max Planck Institute Earth System Model  
17 (MPI-ESM). We conducted a series of inversion experiments, each incorporating JSBACH-generated CH<sub>4</sub> fluxes based on  
18 different CH<sub>4</sub> production Q<sub>10</sub> values, ~~which represents the temperature dependence of CH<sub>4</sub> production to test the temperature~~  
19 ~~sensitivity of emissions~~. Additionally, we examined the impact of changing the baseline  $f_{CH_4}$  fraction value, which defines the  
20 fraction of anaerobically mineralized carbon converted to CH<sub>4</sub>, while keeping all other JSBACH and inversion settings  
21 constant. Our findings show that, at a pan-Arctic scale, using a CH<sub>4</sub> Q<sub>10</sub> value of 1.8 produces the best agreement between the  
22 two approaches. However, no single Q<sub>10</sub> value yielded optimal agreement between the simulated fluxes and the fluxes inferred  
23 from atmospheric observations across all subregions. Instead, the best performance varied spatially, with different CH<sub>4</sub>  
24 production Q<sub>10</sub> values and baseline  $f_{CH_4}$  fraction leading to a better flux agreement in specific areas. These results highlight the  
25 importance of using regionally specific parameters to more accurately estimate wetland CH<sub>4</sub> emissions, and the potential of  
26 employing atmospheric inversions to guide bottom-up process models towards regionally representative parameter settings.

## 27 1. Introduction

28 Methane (CH<sub>4</sub>) is the second most important anthropogenic greenhouse gas and it is emitted from both natural and  
29 anthropogenic sources. Combined wetlands and inland freshwaters are the largest natural source of CH<sub>4</sub> to the atmosphere,  
30 accounting for about 28-37% (by bottom-up and top-down estimates, respectively) of the global total CH<sub>4</sub> emissions (Saunio  
31 et al., 2025). However, quantifying these emissions remains challenging due to the complexity of biogeochemical processes

32 and the spatial variability of these ecosystems. Process-model ensemble estimates indicate that, between 2010 and 2020,  
33 wetlands emitted approximately  $158 \pm 24 \text{ TgCH}_4 \text{ y}^{-1}$ . This represents an increase of  $\sim 5 \text{ TgCH}_4 \text{ y}^{-1}$  compared to the 2000-2009  
34 average, with the most substantial increases observed in tropical regions, followed by mid- and high-latitude areas.  
35 Constraining  $\text{CH}_4$  budgets is particularly relevant in the Arctic-Boreal region, which is warming faster than most other regions  
36 (Rantanen et al., 2022), and at the same time contains extensive wetlands and permafrost landscapes storing significant  
37 amounts of soil carbon (Hugelius et al., 2024). Under warming conditions, this carbon can be mobilized and potentially release  
38 substantial amounts of  $\text{CH}_4$  into the atmosphere. Large uncertainties in Arctic  $\text{CH}_4$  emission estimates limit our ability to  
39 quantify the region's contribution to the global  $\text{CH}_4$  budget and its climate feedbacks.

40 Global and regional  $\text{CH}_4$  emissions are estimated using both bottom-up or top-down approaches. Bottom-up methods,  
41 including inventories, data-driven ecosystem flux upscaling and process-based models, provide detailed information with fine-  
42 scale resolution for both, processes and spatial heterogeneity. Process-based models simulate  $\text{CH}_4$  emissions by mathematically  
43 representing ecosystem dynamics, biogeochemical cycles, and physical processes. However, Nevertheless, it is challenging to  
44 extrapolate these estimates to regional or global scales is challenging due to the strong spatial variability in because wetland  
45 characteristics (e.g., extent, hydrology and vegetation), as well as vary substantially across space, and simulated  $\text{CH}_4$  fluxes  
46 are highly sensitive to the choice of the models to parameterizations. Mechanistic modeling of net surface  $\text{CH}_4$  emissions  
47 requires capturing a range of complex, interacting processes. Top-down approaches estimate net surface-atmosphere  $\text{CH}_4$   
48 fluxes using atmospheric observations (in situ, flask and/or satellite measurements) in combination with prior flux information  
49 (from process-based models and/or inventories), and atmospheric transport and chemistry models to link surface sources with  
50 atmospheric observations. Their ability to provide accurate estimates of net surface-atmosphere fluxes is limited by sparse  
51 observational coverage, particularly in remote regions, as well as by uncertainties in atmospheric transport, prior flux estimates,  
52 and atmospheric  $\text{CH}_4$  sink processes (Houweling et al., 2017). These limitations can lead to significant uncertainties in the  
53 magnitude and spatial distribution of inferred emissions, which makes attributing fluxes to specific sources or processes  
54 challenging. Still, despite these limitations, the inverse modeling approach allowed us to derive important constraints on the  
55 global sources and sinks of  $\text{CH}_4$  (Houweling et al., 2017).

56 Although both approaches are widely used, substantial discrepancies exist between bottom-up and top-down estimates of  
57  $\text{CH}_4$  emissions. From 2010 to 2019, top-down approaches estimated global  $\text{CH}_4$  emissions at  $575 \text{ TgCH}_4 \text{ y}^{-1}$  ( $553\text{-}586 \text{ TgCH}_4$   
58  $\text{y}^{-1}$ ), whereas bottom-up estimates were approximately 15% higher, at  $669 \text{ TgCH}_4 \text{ y}^{-1}$  ( $512\text{-}849 \text{ TgCH}_4 \text{ y}^{-1}$ ) (Saunio et al.,  
59 2025). Similar differences are evident in the high-northern latitudes regions, where wetlands and inland waters dominate  
60 emissions. In the Arctic-Boreal region, bottom-up estimates of  $50 \text{ TgCH}_4 \text{ y}^{-1}$  ( $29\text{-}71 \text{ TgCH}_4 \text{ y}^{-1}$ ) contrast with top-down  
61 estimates of  $20 \text{ TgCH}_4 \text{ y}^{-1}$  ( $15\text{-}24 \text{ TgCH}_4 \text{ y}^{-1}$ ) (Hugelius et al., 2024).

62 Mechanistic modeling of net surface  $\text{CH}_4$  emissions requires capturing a range of complex, interacting processes (Conrad,  
63 1999; Moser et al., 2026; Riley et al., 2011). Anaerobic  $\text{CH}_4$  production is the result of a number of biogeochemical processes  
64 that take place in a chain or in parallel. After an enzymatic breakdown of macromolecules, fermentation of the resulting  
65 dissolved organic matter (DOC) leads to acetate, hydrogen and  $\text{CO}_2$ . In either acetoclastic or hydrogenotrophic

66 ~~methanogenesis, these byproducts are immediately further used to finally produce CH<sub>4</sub> and CO<sub>2</sub>. In addition, alternative~~  
67 ~~electron acceptors, such as Fe-III can be utilized by microbes to produce CO<sub>2</sub> from acetate. As a key parameter, the net~~  
68 ~~CH<sub>4</sub>:CO<sub>2</sub> production ratio is therefore determined by the relative importance of these underlying several biogeochemical~~  
69 ~~processes, which in turn are dependent on environmental conditions, and. That is why in laboratory incubation experiments, a~~  
70 ~~large range of this production ratio has been observed (Knoblauch et al., 2018). As a consequence, After production, CH<sub>4</sub> may~~  
71 ~~be consumed by methanotrophic bacteria or transported to the atmosphere via plant aerenchyma, ebullition, or diffusion~~  
72 ~~through soil or water. That leads to a CH<sub>4</sub>:CO<sub>2</sub> emission ratio at the surface which is different from the CH<sub>4</sub>:CO<sub>2</sub> production~~  
73 ~~ratio. Since underlying biogeochemical processes are very complex and dependent on detailed environmental conditions,~~  
74 ~~global-scale land surface models often usually represent anaerobic CH<sub>4</sub> production in a simplified way, i.e. as a first-order~~  
75 ~~decay of soil organic matter with adjusted rate constants, applying. And then, a fixed ratio of CH<sub>4</sub> versus CO<sub>2</sub> production out~~  
76 ~~of that decomposition is applied (Guimbertau et al., 2018; Kleinen et al., 2020; Moser et al., 2026; Ricciuto et al., 2021; Sellar~~  
77 ~~et al., 2019). Here, the models can differ in whether the ratio applies to the CH<sub>4</sub> production or emission. The JSBACH v3.2~~  
78 ~~that we apply in this study is taking the first approach and mechanistically distinguish between methanogenesis and~~  
79 ~~methanotrophy.~~

80 ~~Developing these Biogeochemical process models requires balancing the inclusion of key mechanisms with limitations~~  
81 ~~such as structural and parameter uncertainty, spatial heterogeneity, sparse observational data, uncertain initial and boundary~~  
82 ~~conditions, and computational constraints (Riley et al., 2011). Previous studies have shown that Regarding the simulation of~~  
83 ~~CH<sub>4</sub> emissions, are highly sensitive to parameters regulating microbial production and oxidation processes. A a higher~~  
84 ~~CH<sub>4</sub>:CO<sub>2</sub> ratio indicates a greater dominance of CH<sub>4</sub> in production and emission relative to CO<sub>2</sub> (Chinta et al., 2024), while~~  
85 ~~Based on anaerobic incubations of thermokarst lake sediments, observed that the  $\Delta^{14}\text{C}$  values of both CH<sub>4</sub> and CO<sub>2</sub> showed~~  
86 ~~strong positive correlations with net CH<sub>4</sub> production rates and CH<sub>4</sub>:CO<sub>2</sub> ratios. This indicates that CH<sub>4</sub> production occurs faster~~  
87 ~~and at a higher rate when younger organic matter decomposes. These patterns suggest that the presence of younger carbon~~  
88 ~~substrates increases methanogenesis compared to overall fermentation and anaerobic respiration. A a higher CH<sub>4</sub> production~~  
89 ~~Q<sub>10</sub> indicates that CH<sub>4</sub> production increases more rapidly with rising temperatures. This can indirectly enhance diffusive fluxes~~  
90 ~~by creating larger concentration gradients between the soil and the atmosphere. However, As regional model sensitivity~~  
91 ~~varies and site-specific measurements may not be representative across broader areas, both the CH<sub>4</sub>:CO<sub>2</sub> ratio and the CH<sub>4</sub>~~  
92 ~~production Q<sub>10</sub> are uncertain at large spatial scales. For example, increasing CH<sub>4</sub> production Q<sub>10</sub> in high-latitude regions can~~  
93 ~~reduce simulated CH<sub>4</sub> emissions by more than half, because the temperature-dependent component, scaled relative to a~~  
94 ~~reference temperature of 295 K, leads to a decline in CH<sub>4</sub> production rate at the lower temperatures typical of these regions~~  
95 ~~(Riley et al., 2011). As m Many large-scale land surface models still rely on simplified, fixed CH<sub>4</sub> production fractions, which~~  
96 ~~limits their ability to accurately represent observed spatiotemporal variability in CH<sub>4</sub>:CO<sub>2</sub> production ratios across Arctic~~  
97 ~~landscapes is therefore limited (Moser et al., 2026). These differences in model structure, parameterization and initialization~~  
98 ~~contribute strongly to relative high uncertainties in wetland estimates (Poulter et al., 2017).~~

99 The JSBACH v3.2 model (Reick et al., 2021) that we apply in this study is taking the first approach and mechanistically  
100 distinguish between methanogenesis and methanotrophy. In JSBACH v3.2, anaerobic decomposition and CH<sub>4</sub> oxidation are  
101 temperature dependent, and. However, in addition to that, the CH<sub>4</sub>:CO<sub>2</sub> production ratio is also assumed to follow a Q<sub>10</sub>  
102 temperature sensitivity (Kleinen et al., 2020). That means that we assume thatThis formulation allows the relative importance  
103 of the above-mentioned underlying biogeochemical processes changes in space and time depending on the soil temperature.  
104 In addition, making the CH<sub>4</sub>:CO<sub>2</sub> production ratio temperature dependent allows us to additionally tune CH<sub>4</sub> versus CO<sub>2</sub>  
105 production across bioclimatic zones. Still, the optimum parameter setting of One big research question now is, how high should  
106 be the Q<sub>10</sub> value for this temperature dependency of the CH<sub>4</sub>:CO<sub>2</sub> production ratio is still highly uncertain. In order to answer  
107 such question, we employ a novel integration of bottom-up and top-down approaches.

108 Top-down approaches estimate net surface atmosphere CH<sub>4</sub> fluxes using atmospheric observations (in situ, flask and/or  
109 satellite measurements) in combination with prior flux information (from process-based models and/or inventories), and  
110 atmospheric transport and chemistry models to link surface sources with atmospheric observations. Their ability to provide  
111 accurate estimates of net surface atmosphere fluxes is limited by sparse observational coverage, particularly in remote regions,  
112 as well as by uncertainties in atmospheric transport, prior flux estimates, and atmospheric CH<sub>4</sub> sink processes. These  
113 limitations can lead to significant uncertainties in the magnitude and spatial distribution of inferred emissions, which makes  
114 attributing fluxes to specific sources or processes challenging. Still, despite these limitations, the inverse modeling approach  
115 allowed us to derive important constraints on the global sources and sinks of CH<sub>4</sub>.

116 Substantial discrepancies exist between bottom-up and top-down estimates of CH<sub>4</sub> emissions. From 2010 to 2019, top-  
117 down approaches estimated global CH<sub>4</sub> emissions at 575 TgCH<sub>4</sub> y<sup>-1</sup> (553–586 TgCH<sub>4</sub> y<sup>-1</sup>), whereas bottom-up estimates were  
118 approximately 15% higher, at 669 TgCH<sub>4</sub> y<sup>-1</sup> (512–849 TgCH<sub>4</sub> y<sup>-1</sup>). These differences, despite the fact that bottom-up results  
119 are used as prior in top-down approaches, point to additional constraints of bottom-up CH<sub>4</sub> flux estimates by atmospheric  
120 observations. For example, important large-scale CH<sub>4</sub> uptake by upland soils is usually underrepresented in land surface  
121 models. More generally, we assume that bottom-up approaches are still very limited in their ability to upscale the complex  
122 and spatially varying processes underlying CH<sub>4</sub> emissions. In boreal regions, inland freshwater sources dominate CH<sub>4</sub>  
123 emissions, accounting for 41% and 54% in top-down and bottom-up budgets, respectively. Similarly, reported substantial  
124 discrepancies between bottom-up and top-down CH<sub>4</sub> emission estimates for the Arctic boreal region, with 50 TgCH<sub>4</sub> y<sup>-1</sup> (29–  
125 71 TgCH<sub>4</sub> y<sup>-1</sup>) for bottom-up and 20 TgCH<sub>4</sub> y<sup>-1</sup> (15–24 TgCH<sub>4</sub> y<sup>-1</sup>) for top-down. Despite recent efforts to improve monitoring  
126 networks and modeling frameworks, significant discrepancies remain between these approaches. Still, top-down approaches  
127 can be used to assess the representativeness of bottom-up fluxes and their underlying parameterizations on a large scale.  
128 Combining information from both methods can therefore help to reconcile discrepancies and improve the consistency of CH<sub>4</sub>  
129 emission estimates at different spatial scales.

130 This study therefore explores novel concepts the for usage of atmospheric inverse modeling to constrain parameter  
131 settings in bottom-up estimates of wetland CH<sub>4</sub> emissions in the Arctic-Boreal region. Using the Jena CarboScope global  
132 inversion system, we employed prior fluxes from the JSBACH land surface model (a component of the MPI Earth System

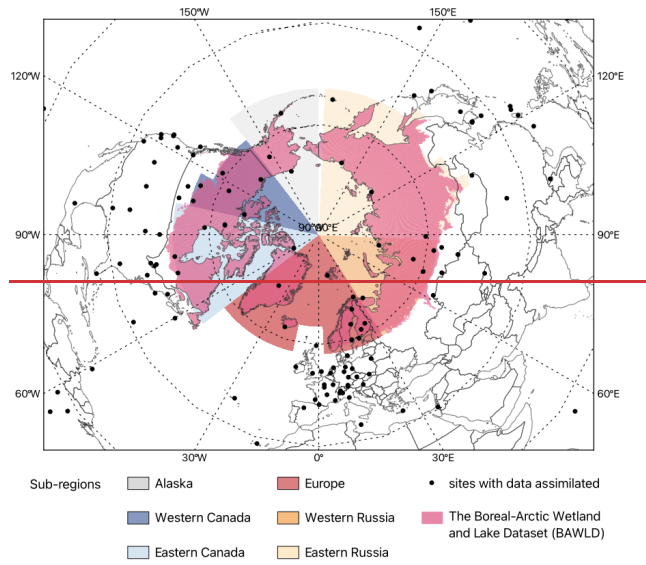
133 Model) and systematically varied key parameters that govern CH<sub>4</sub> production. Specifically, we tested a range of Q<sub>10</sub> values,  
134 which define the temperature sensitivity of CH<sub>4</sub> production, and different  $f_{CH_4}$  baseline values, which determine the proportion  
135 of anaerobically mineralized carbon converted to CH<sub>4</sub>. However, a portion of the produced CH<sub>4</sub> is oxidized to CO<sub>2</sub>. Since  
136 transport pathways determine how much CH<sub>4</sub> is exposed to oxidation on its way to the surface, they reduce the resulting  
137 CH<sub>4</sub>:CO<sub>2</sub> emission ratio. We kept other model settings constant throughout these tests. Integrating these parameter sensitivity  
138 experiments into the inversion framework allowed us to assess which parameterizations yield the most consistent fluxes with  
139 atmospheric observations. This approach enables us to identify regionally representative parameter settings and guide  
140 parameterizations that could improve the consistency between bottom-up process models and top-down constraints on Arctic-  
141 Boreal wetland CH<sub>4</sub> emissions.

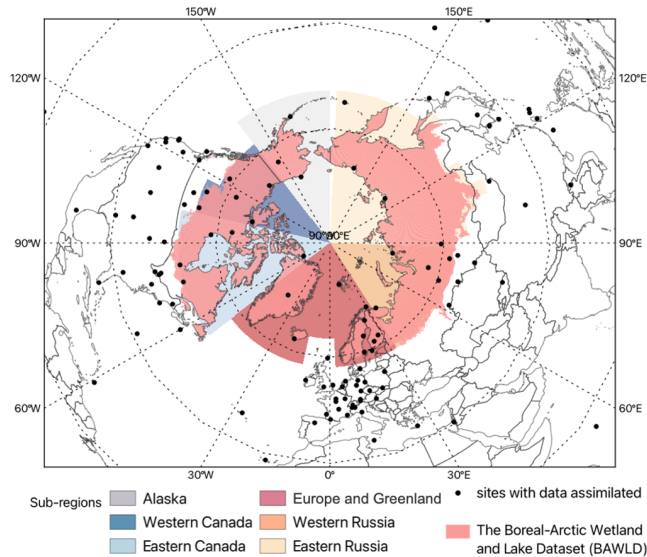
## 142 2. Methods

### 143 2.1. Region and time period of interest

144 Our Arctic-Boreal domain was defined based on The Boreal-Arctic Wetland and Lake Dataset – BAWLD (Olefeldt et al.,  
145 2021), and we divided this region into 6 sub-regions for more detailed spatial analyses (Alaska, western Canada, eastern  
146 Canada, Europe including Greenland, western Russia, eastern Russia, Fig. 1). In recent decades, the atmospheric observation  
147 network suitable for inverse modeling has expanded across the Arctic, with a considerable increase in available sites after 2010  
148 (Vogt et al., 2025). However, due to data-sharing disruptions associated with the ongoing conflict involving Russia and  
149 Ukraine, observational data from Russian stations has been limited since 2022. Consequently, this study focuses on the period  
150 from 2010 to 2021, when data coverage from surface stations was more consistent across the full domain.

151





153

154 Figure 1: Geographic distribution of surface sites operated by different network providers where flask-based and/or continuous  
 155 in-situ CH<sub>4</sub> measurements are available for assimilation into the inverse model (black dots; [Supplementary Table 1](#)). The  
 156 colored boxes delineate the Arctic-Boreal regions (Alaska, western Canada, eastern Canada, Europe [including Greenland](#),  
 157 western Russia, eastern Russia), as defined based on The Boreal–Arctic Wetland and Lake Dataset (BAWLD) (Olefeldt et al.,  
 158 2021).

## 159 2.2. Wetland estimates used as prior fluxes in the inverse modelling

160 In this study, we utilize the JSBACH model (Reick et al., 2021), the land component of the MPI-ESM (Mauritsen et al.,  
 161 2019), to estimate bottom-up wetland CH<sub>4</sub> emissions. ~~Originally, JSBACH is run in was developed as a lower boundary~~  
 162 ~~condition for the atmospheric component of the MPI-ESM; however, it has since been updated to function as a standalone~~  
 163 ~~mode at land surface model driven by observed climate data to simulate terrestrial components of the carbon, energy and water~~  
 164 ~~cycles. In this study, simulations conducted at T63 resolution (approximately 1.85°, or 185 km) were and driven using the by~~  
 165 ~~CRUJRA2.3 (Harris, 2019) climate data forcing. Soil hydrology and thermodynamics follow the A-multilayer vertical soil~~  
 166 ~~profile is implemented as described by formulation of Hagemann and Stacke (2015), while with features relevant for high-~~  
 167 ~~northern latitudes permafrost-related processes implemented as described by have been implemented by Ekici et al. (2014).~~

168 ~~The Richards' equation, along with thermal diffusion, governs the vertical distribution of moisture and heat in the soil.~~ Soil  
169 organic carbon (SOC) decomposition is simulated as a first-order decay process that depends on surface air temperature, water  
170 availability, and litter size, following the YASSO model formulation (Tuomi et al., 2011) and its implementation in JSBACH  
171 by Goll et al. (2015).

172 The wetland area fraction of the grid is determined using TOPMODEL (Beven and Kirkby, 1979), a conceptual rainfall-  
173 runoff model that estimates inundation based on the compound topographic index (CTI). If the inundated fraction of the grid  
174 is non-frozen (depending on the soil temperature), it is considered a CH<sub>4</sub>-emitting area. The methodology for wetland CH<sub>4</sub>  
175 production and transport is adopted from Riley et al. (2011), and the details of the TOPMODEL and its implementation for  
176 wetland CH<sub>4</sub> within JSBACH are outlined in Kleinen et al. (2020). ~~TOPMODEL assumes a constant exponential decline of~~  
177 ~~transmissivity with depth, defined as the ratio of the difference between the local sub-grid-scale CTI and the mean grid-cell~~  
178 ~~CTI to the difference between their corresponding local sub-grid-scale water table and mean grid-cell water table (see equation~~  
179 ~~(1) in As water propagates from the surface, it saturates the soil layers based on volumetric moisture content and field capacity.~~  
180 ~~Starting from the bottom of the soil column, the mean grid-cell water table is located in the first soil layer where the layer~~  
181 ~~saturation is below the experimentally determined saturation threshold. The sensitivity study indicates that using CRUJRA as~~  
182 ~~the forcing data, setting the saturation threshold at 7.25, configuring the exponential decline of transmissivity with depth to 4,~~  
183 ~~and limiting the valid range of CTI to values greater than 5.5 results in a reasonable estimation of present-day wetland extents.~~

184 In JSBACH, carbon enters the soil as litter, both above- and belowground, originating from decomposing vegetation. This  
185 carbon eventually returns to the atmosphere through decomposition processes as CO<sub>2</sub> and CH<sub>4</sub> emissions. Carbon fixed by  
186 vegetation is allocated to green tissue (leaves, fine roots), wood (stems, branches), and reserve pools (e.g., sugars and starches).  
187 Routine turnover, herbivory, and root exudation transfer carbon into above- and belowground litter pools. Depending on the  
188 plant functional type (PFT), litter carbon is distributed among acid-soluble, water-soluble, ethanol-soluble, and non-soluble  
189 pools, each further divided into above- and belowground fractions, as well as a humus pool. Decomposition rates vary based  
190 on temperature, precipitation, and litter size. Under anoxic conditions (in the inundated fraction of the tile), SOC decomposes  
191 into both CO<sub>2</sub> and CH<sub>4</sub>. The baseline rate of SOC decomposition under anaerobic conditions is reduced compared to aerobic  
192 conditions. Temperature dependency of CH<sub>4</sub> production as part of SOC decomposition follows the Q<sub>10</sub> model with a reference  
193 temperature of 295K (Equation 1).

194 Methane production and the transport pathways that move CH<sub>4</sub> to the surface (diffusion, plant-mediated aerenchyma and  
195 ebullition) follow the scheme of Riley et al. (2011), as implemented in JSBACH by Kleinen et al. (2020). Under anaerobic  
196 conditions, a proportion of SOC ( $f_{CH_4}$ ) is converted to CH<sub>4</sub>, while the remaining is converted to CO<sub>2</sub>. The temperature  
197 dependence of  $f_{CH_4}$  is represented using a Q<sub>10</sub> formulation.

$$198 \quad f_{CH_4} = f_{CH_4,baseline} \cdot Q_{10}^{(T_{soil}-295)/10K} \quad \text{Equation 1}$$

199 The fraction of CH<sub>4</sub> production is capped at 0.5; that is, no more than 50% of carbon can be converted to CH<sub>4</sub>. However, the  
200 CH<sub>4</sub>:CO<sub>2</sub> ratio of net emissions to the atmosphere is typically lower than the ratio of gross production due to oxidation

(methanotrophy) and differences in transport pathways. Oxidation, which follows Michaelis-Menten kinetics (with  $Q_{10} = 1.9$ , which remained constant throughout the sensitivity tests), converts a portion of  $CH_4$  to  $CO_2$ , thus increasing  $CO_2$  and decreasing  $CH_4$  emissions. Transport mechanisms further differentiate the fate of these gases:  $CH_4$  can escape via diffusion, plant-mediated transport, or ebullition, whereas  $CO_2$  is not released through ebullition.  $O_2$  availability and soil moisture regulate the efficiency of  $CH_4$  oxidation. Therefore, the net  $CH_4:CO_2$  emission ratio depends on the combined effects of  $CH_4$  production, oxidation, and transport processes. Warmer, oxic conditions tend to reduce the net  $CH_4:CO_2$  (due to stronger aerobic oxidation of  $CH_4$ ), while colder or persistently anoxic, saturated conditions (with ebullition) can increase the net  $CH_4:CO_2$  ratio compared to cases with strong oxidation. Equation 1 shows how the  $Q_{10}$  law controls the  $CH_4$  fraction ( $f_{CH_4}$ ) as a function of soil temperature ( $T_{soil}$ ) and the baseline fraction (baseline  $f_{CH_4}$  fraction):

Oxidation reduces the amount of  $CH_4$  that reaches the atmosphere. Consequently, the net  $CH_4:CO_2$  emission ratio depends on production and oxidation rates, as well as transport pathways, which control the amount of  $CH_4$  exposed to oxidation. A simplified conceptual relationship is as follows:

$$CH_4:CO_2 = \frac{f_{CH_4}P - O_{CH_4}}{(1-f_{CH_4})P + O_{CH_4}} \quad \text{Equation 2}$$

where P is gross anaerobic SOC decomposition and O is the amount of  $CH_4$  oxidized before emission.

To evaluate how sensitive  $CH_4$  wetland emission estimates are to key parameters, we conducted nine experiments in which we varied only the  $Q_{10}$  coefficient for  $CH_4$  production and the baseline  $f_{CH_4}$  fraction (Fig. 2b). Specifically, we tested three different  $Q_{10}$  values ranging from 1.4 to 2.2, consistent with commonly used values reported in literature review (Moser et al., 2026), and baseline  $f_{CH_4}$  fractions from 0.33 to 0.38. These combinations are summarized in Table 1 and were chosen to identify parameter sets that best align with the observed atmospheric data. All other carbon decomposition, hydrological, transport, and oxidation processes follow the standard JSBACH configuration.

### 2.3. Inverse modeling setup

We used the Jena CarboScope Inversion System (Rödenbeck, 2005) to quantify  $CH_4$  emissions between the surface and the atmosphere globally from 2010 to 2021, with the evaluation and interpretation of fluxes focused on the Arctic-Boreal region. This is a linear Bayesian framework that infers surface-atmosphere  $CH_4$  fluxes by combining prior flux estimates with atmospheric  $CH_4$  mole fraction measurements and accounting for their respective uncertainties based on observed atmospheric mole fractions. The flux vector  $f$  represents the net flux per grid cell per time step. The Jena CarboScope enables  $f$  to be

Formatted: Indent: First line: 0 cm

Formatted: Border: Top: (No border), Bottom: (No border), Left: (No border), Right: (No border)

232 represented as the sum of different flux components, each of which is modelled independently using its own statistical linear  
233 flux model. These independent a priori error covariance structures allow deviations from the prior flux estimate to be attributed  
234 to specific components during the inversion process. In this study, the a priori shape uncertainty was defined as 100% of the  
235 prior flux for each flux category. All flux categories were optimized, assuming spatial correlation lengths of ~500 km and  
236 temporal correlation lengths of about 15 days. Temporal and spatial fluxes are optimized within a Bayesian inversion  
237 framework that minimizes a cost function combining prior and observational constraints. The solution is obtained analytically  
238 using the linear Bayesian approach, which yields maximum posterior flux estimates and their associated uncertainties. Details  
239 of the cost function formulation and solution method can be found in the CarboScope technical report (Rödenbeck, 2005).

240 A total of 154 stations were assimilated for the global domain (Fig. 1; [Supplementary Table 1](#)). These CH<sub>4</sub> observations  
241 were obtained from ~~several~~-multiple global and regional networks (ICOS RI et al., 2024; Panov et al., 2021; Sasakawa et al.,  
242 2010, 2025; Schuldt et al., 2023), with the majority of sites located in the Northern Hemisphere, including 33 stations within  
243 the Arctic-Boreal domain. ~~Most observational data used in this study were accessed through NOAA GML ObsPack (Schuldt~~  
244 ~~et al., 2023), ICOS Carbon Portal (ICOS RI et al., 2024), World Data Centre for Greenhouse Gases (WDCGG) database~~  
245 ~~([https://doi.org/10.50849/WDCGG\\_CH4\\_ALL\\_2023](https://doi.org/10.50849/WDCGG_CH4_ALL_2023)), and JR-STATION network (Sasakawa et al., 2010, 2025); further~~  
246 ~~details are provided in the “Data Availability section”. Detailed information on the stations with assimilated data is given in~~  
247 ~~Supplementary Table 1.~~ For tower sites with multiple intake heights available, we assimilated only data from the highest height  
248 in the inversion, and for the continuous data, we use only daytime measurements. The transport model used in CarboScope is  
249 the TM3 global atmospheric tracer model, an Eulerian transport model that solves the continuity equation (and  
250 parameterizations of boundary layer and convective mixing) for atmospheric tracers in a three-dimensional grid over the globe  
251 (Heimann and Körner, 2003). ~~and~~ The model has a spatial resolution of approximately 3.8° latitude by 5° longitude, with 19  
252 vertical layers, and it is driven by meteorological inputs from the NCEP reanalysis dataset (Kalnay et al., 1996). Flux inversions  
253 were conducted at the TM3 spatial resolution—a spatial resolution of approximately 3.8° latitude by 5° longitude, with 19 vertical  
254 layers and a daily temporal resolution. Since the model is initialized with a homogeneous background concentration of  
255 methane, it is run for at least one year before to the period of interest to avoid any impact resulting from the model spin-up.  
256 To account for model-data mismatch, including the representation error of the measurements within the transport model, each  
257 station is assigned a weekly error value based on how well the atmospheric transport model can capture local atmospheric  
258 dynamics. For example, for mountain sites and stations near shores samples are assigned a smaller error of 15 ppb, whereas  
259 surface sites in regions with complex circulation patterns receive a larger error of 30 ppb~~we assigned an uncertainty of 30 ppb.~~  
260 Additionally, to ensure balanced representation across observational sites, particularly between continuous and sparse time  
261 series, we applied a data density weighting scheme, assigning equal influence to each weekly period, regardless of data  
262 frequency. Without this adjustment, sites with high-frequency data would dominate the cost function solely because of the  
263 greater number of observations. To avoid this, the uncertainty of each measurement is multiplied by the number of observations  
264 per week. This corresponds to the assumption that errors are correlated on weekly timescales, meaning that one week of hourly  
265 data provides roughly the same amount of independent information as one weekly flask sample (Rödenbeck, 2005).

Field Code Changed

266 Prior CH<sub>4</sub> flux estimates include five source categories, all of which were optimized: wetlands, other natural sources,  
267 anthropogenic, ocean and fire emissions. The monthly mean emissions from wetlands and fires were obtained from the  
268 JSBACH model (Kleinen et al., 2020), as previously described. Fire emissions represent the simulated biomass burning  
269 emissions of JSBACH and were prescribed as monthly varying prior fluxes. Additional natural sources, such as termites and  
270 wild animal emissions taken from JSBACH (Kleinen et al., 2020) and geological emissions from Etiope et al. (2019) were  
271 combined as the “other natural source” category. Emissions from oceans were obtained from Weber et al. (2019) and  
272 implemented as a non-seasonal climatology. Anthropogenic emissions were obtained from the EDGAR inventories database  
273 (<https://edgar.jrc.ec.europa.eu>) version 8 (Crippa et al., 2023) and are provided as monthly global fluxes. This category  
274 includes emissions from agriculture, livestock, waste management, fossil fuel exploitation and other minor anthropogenic  
275 sources except biomass burning. Emissions of CH<sub>4</sub> from inland water (freshwater) were not included as a separate prior  
276 category and are therefore not explicitly optimized in the inversion framework.

277 CH<sub>4</sub> chemical loss includes loss due to OH and Cl in the troposphere, as well as OH, Cl, and O(<sup>1</sup>D) in the stratosphere.  
278 For tropospheric OH, we use the monthly three-dimensional OH fields calculated by Spivakovsky et al. (2000), which are  
279 based on observed climatological distributions of OH precursors and scaled to match the observed CH<sub>3</sub>CCl<sub>3</sub> lifetime. The  
280 monthly climatological loss rates of CH<sub>4</sub> in the stratosphere due to OH, Cl, and O(<sup>1</sup>D) were derived from a simulation of the  
281 ECHAM5/MESy1 chemistry transport model (Jöckel et al., 2006). Additionally, tropospheric Cl loss is simulated using a  
282 recent model-derived estimate of tropospheric Cl (Hossaini et al., 2016). The surface sink from upland soils and the ocean was  
283 implemented as a zeroth-order reaction with prescribed reaction rates that occur only in the surface-most model layer. Reaction  
284 rates for the microbial oxidation of atmospheric CH<sub>4</sub> in soil were based on the uptake estimates from the LPJ-Bern model  
285 (Spahni et al., 2011).

#### 286 **2.4. Evaluating Bottom-Up Emissions Using Top-Down Constraints**

287 Previous studies have used atmospheric inversion models to evaluate ~~in-between~~ different bottom-up estimates and  
288 determine which one best reproduces observed atmospheric CH<sub>4</sub> data (Kim et al., 2011; Miller et al., 2016), providing an  
289 effective framework for model evaluation. In this study, we evaluated the performance of different JSBACH parameterizations  
290 by using the CH<sub>4</sub> wetland emission outputs from each experiment as wetland prior fluxes in a top-down atmospheric inversion  
291 framework. The inversion then generated posterior fluxes, reflecting the adjustments needed to align the prior emissions with  
292 atmospheric CH<sub>4</sub> observations. These adjustments take into account uncertainties in atmospheric transport, observational  
293 errors, and model representation. In this study, we used the model adjustment defined as the difference between posterior and  
294 prior fluxes, calculated as the mean monthly and mean annual values across the Arctic–Boreal region from 2010 to 2021. First,  
295 we identified the parameterization resulting in the lowest mean model adjustment across the entire domain.

296 For the monthly analysis, we first computed the mean monthly prior flux and the mean monthly posterior flux, and then  
297 defined the model adjustment as the difference between these two means. For the annual analysis, we calculated the mean

298 annual prior and posterior fluxes and again defined the adjustment as their difference. This allowed us to determine which  
 299 JSBACH configuration provided the best overall agreement with atmospheric constraints at the pan-regional scale and  
 300 investigate temporal variability.

301 Next, we examined spatial variability of the difference between posterior and prior fluxes using different JSBACH  
 302 parameterizations as wetland priors. At the grid-cell level, we identified the parameter combination that minimized annual  
 303 model adjustment, thereby providing the best match to the top-down atmospheric constraints. To conduct this analysis, an  
 304 ensemble of posterior fluxes was calculated based on each CH<sub>4</sub> production Q<sub>10</sub> value from the prior wetland flux. This approach  
 305 was supported by the observation that CH<sub>4</sub> production Q<sub>10</sub> significantly influenced CH<sub>4</sub> emission estimates compared to the  
 306 baseline  $f_{CH_4}$  fraction. Additionally, posterior fluxes from priors with different baseline  $f_{CH_4}$  fraction scenarios remained highly  
 307 similar for a given Q<sub>10</sub> value. As a result, maps were ~~made~~ created by calculating the absolute difference between the posterior  
 308 ensemble of the respectively Q<sub>10</sub> value and prior CH<sub>4</sub> fluxes for each experiment at each grid-cell. Then, the annual mean  
 309 adjustment was calculated and we identified the parameterization that resulted in the smallest adjustment at each grid-cell. In  
 310 summary, each grid-cell shows the experiment that best matched the atmospheric CH<sub>4</sub> observations.

### 311 3. Results and Discussion

#### 312 3.1 Sensitivity of JSBACH CH<sub>4</sub> wetland emission estimates to CH<sub>4</sub> production Q<sub>10</sub> and baseline $f_{CH_4}$ fraction in the 313 Arctic-Boreal region

314 Table 1 summarizes the experiments and parameters combinations that have been tested in the JSBACH model and used  
 315 as a wetland prior in the atmospheric inversions. Across the Arctic-Boreal region, our nine experiments produced annual mean  
 316 CH<sub>4</sub> wetland estimates ranging from 13.8 to 33.5 TgCH<sub>4</sub> y<sup>-1</sup>. These estimates are consistent with previously published bottom-  
 317 up estimates of ~15-50 TgCH<sub>4</sub> y<sup>-1</sup> ~~per year~~, with most studies reporting mean values near 20-25 TgCH<sub>4</sub> y<sup>-1</sup> (Christensen et al.,  
 318 1996; Ying et al., 2025; Yuan et al., 2024; Zhang et al., 2025). It should be noted that these studies consider different spatial  
 319 domains and time periods. The estimates obtained using a Q<sub>10</sub> value of 1.8 align most closely with this published range among  
 320 our experiments.

321  
 322 Table 1. Summary of JSBACH wetland CH<sub>4</sub> estimates used as prior fluxes in the inversions and posterior fluxes estimates for  
 323 each respective model run.

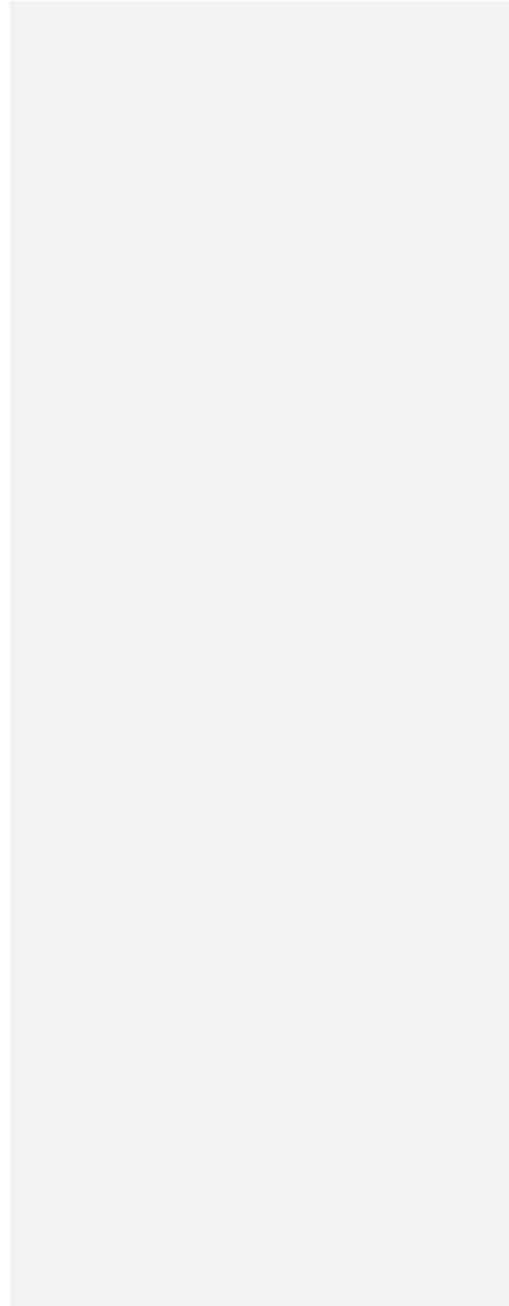
| JSBACH parameterization      |                       | Arctic-Boreal annual mean CH <sub>4</sub> emission (TgCH <sub>4</sub> y <sup>-1</sup> )* |                     |                       |
|------------------------------|-----------------------|------------------------------------------------------------------------------------------|---------------------|-----------------------|
| Baseline $f_{CH_4}$ fraction | Q <sub>10</sub> model | JSBACH estimates (prior)                                                                 | Posterior estimates | Mean model adjustment |
| 0.33                         | 1.4                   | 31.7 ± 1.1                                                                               | 25.0 ± 1.4          | -6.7                  |
| 0.33                         | 1.8                   | 20.0 ± 0.7                                                                               | 22.9 ± 1.1          | 2.9                   |
| 0.33                         | 2.2                   | 14.6 ± 0.5                                                                               | 21.2 ± 0.9          | 6.6                   |

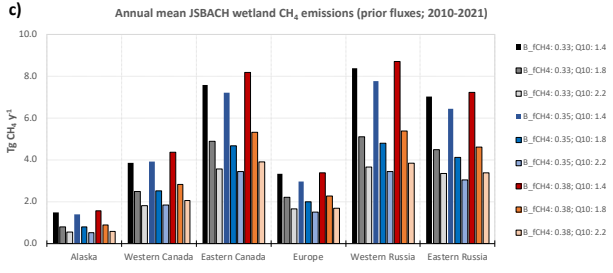
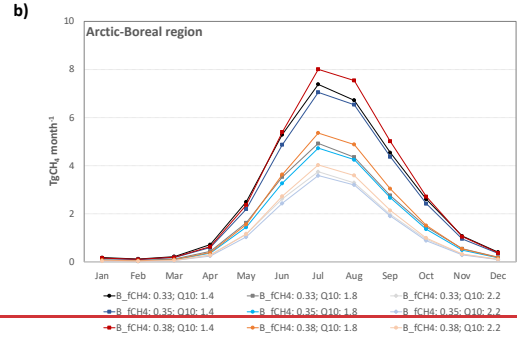
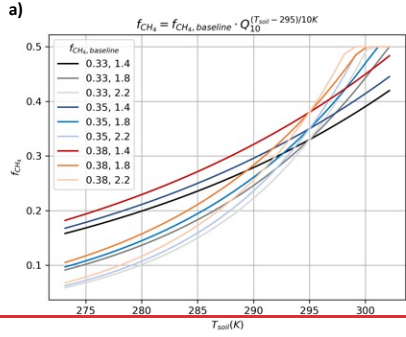
|      |     |            |            |      |
|------|-----|------------|------------|------|
| 0.35 | 1.4 | 29.7 ± 0.9 | 24.8 ± 1.5 | -5.0 |
| 0.35 | 1.8 | 18.9 ± 0.6 | 22.7 ± 1.1 | 3.8  |
| 0.35 | 2.2 | 13.8 ± 0.5 | 20.9 ± 0.9 | 7.1  |
| 0.38 | 1.4 | 33.5 ± 1.0 | 25.2 ± 1.6 | -8.2 |
| 0.38 | 1.8 | 21.3 ± 0.7 | 23.3 ± 1.2 | 2.0  |
| 0.38 | 2.2 | 15.5 ± 0.5 | 21.6 ± 1.0 | 6.1  |

\*The annual mean between 2010 and 2021, with the standard deviation representing interannual variability.

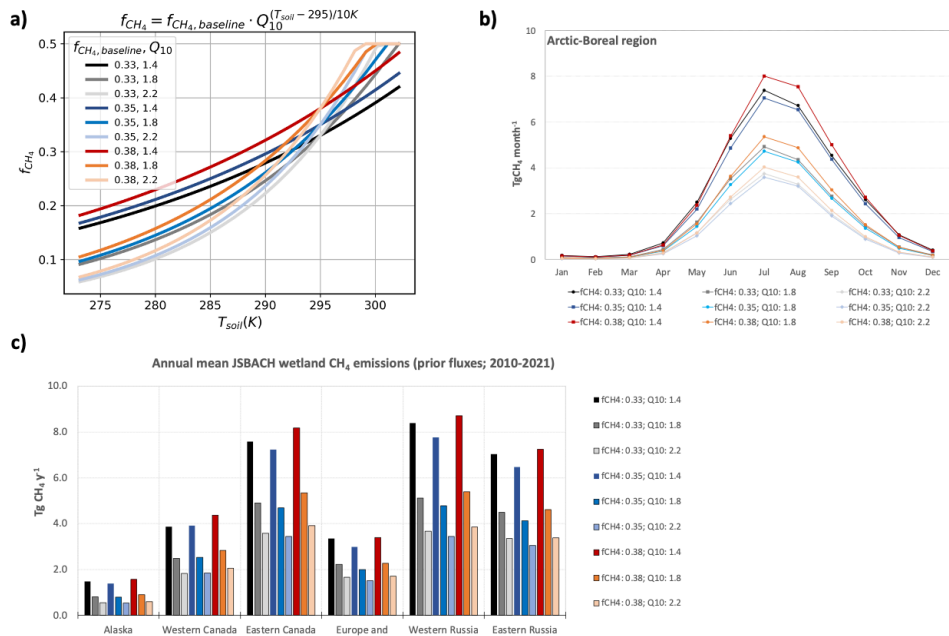
Emissions peaked during the summer months (July-August), with a mean emission ranging from 6.8 to ~~14.4~~15.5 TgCH<sub>4</sub> y<sup>-1</sup> (Fig. 2b). These larger emissions were followed by spring (May-June; range of 3.5-7.8 TgCH<sub>4</sub> y<sup>-1</sup>), autumn (September-October; range of 2.8-7.7 TgCH<sub>4</sub> y<sup>-1</sup>), and winter with the lower emissions (November-April; range of ~~0.74-2.74~~5 TgCH<sub>4</sub> y<sup>-1</sup>). The timing of the peak in wetland emissions aligns with previous bottom-up estimates (Ying et al., 2025). At the sub-regional scale, emissions showed substantial spatial variability (Fig. 2c). The highest annual mean fluxes were found in western Russia (3.4-8.7 TgCH<sub>4</sub> y<sup>-1</sup>, depending on the parameter set), followed by eastern Canada (3.4-8.2 TgCH<sub>4</sub> y<sup>-1</sup>), eastern Russia (3.1-7.2 TgCH<sub>4</sub> y<sup>-1</sup>), western Canada (1.8-4.4 TgCH<sub>4</sub> y<sup>-1</sup>), Europe including Greenland (1.5-3.4 TgCH<sub>4</sub> y<sup>-1</sup>), and Alaska (0.5-1.6 TgCH<sub>4</sub> y<sup>-1</sup>).

In general, increasing the baseline value of the  $f_{CH_4}$  fraction from 0.33 to 0.38 increases CH<sub>4</sub> production. However, an increase in the CH<sub>4</sub> production Q<sub>10</sub> parameter decreases CH<sub>4</sub> production for temperatures below 295 K (the reference temperature) and increases it for temperatures higher than 295 K. This means that increasing Q<sub>10</sub> values from 1.4 to 2.2 reduces wetland CH<sub>4</sub> emissions in the comparatively cold Arctic region (Table 1 and Fig. 2). The sensitivity of wetland CH<sub>4</sub> to the Q<sub>10</sub> temperature response and the baseline  $f_{CH_4}$  fraction is evident when comparing seasonal cycles over the Arctic-Boreal domain (Fig. 2b). For example, contrasting the simulations with baseline  $f_{CH_4}$  fraction equaling 0.33 and varying CH<sub>4</sub> production Q<sub>10</sub> values (from 1.4 to 2.2), shows that increasing Q<sub>10</sub> significantly reduces annual wetland mean CH<sub>4</sub> emission in this region by ~54% (~17 TgCH<sub>4</sub> y<sup>-1</sup>). This reduction is not uniform throughout the year. Although winter emissions are relatively low, increasing Q<sub>10</sub> from 1.4 to 2.2 results in a ~~~70~~2% decrease compared to a ~50-59% decrease during the summer, spring and fall. Similarly, the influence of the baseline  $f_{CH_4}$  fraction can be observed by keeping Q<sub>10</sub> constant, for example at 1.4, and varying the baseline  $f_{CH_4}$  fraction from 0.33 to 0.38. This increase leads to an increase of up to 6% in the annual wetland CH<sub>4</sub> emissions for the region. In general, our parameter sensitivity tests show that CH<sub>4</sub> production Q<sub>10</sub> has a stronger effect on emission variability than the baseline  $f_{CH_4}$  fraction. These wetland CH<sub>4</sub> emission estimates with different parameterizations were subsequently integrated into the Jena CarboScope atmospheric inversion framework as wetland prior fluxes to determine the combination that closest align with atmospheric CH<sub>4</sub> observations, which means those requiring the minimum adjustment to fluxes from prior to posterior.





351



352 Figure 2. a) Sensitivity of  $f_{CH_4}$  production fraction to the chosen range of input parameters for this study. The y-axis represents  
 353 the fraction of anaerobic carbon mineralization allocated to  $CH_4$  production, calculated using the equation displayed at the top  
 354 of the panel and in Equation 1. In the legend, the first number denotes the  $f_{CH_4}$  baseline fraction and the second number denotes  
 355 the  $CH_4$  production  $Q_{10}$  value. b) Mean seasonal cycle of Arctic-Boreal wetland  $CH_4$  emissions for each experiment used in  
 356 the inversion as the wetland prior flux. c) Annual mean wetland fluxes from each experiment estimated by JSBACH model.  
 357  
 358

### 3.2 Evaluation of JSBACH $CH_4$ Fluxes Using Inverse Modeling

359 Our nine inverse model estimates produce an annual mean total emission (i.e. including natural and anthropogenic  
 360 sources) for the Arctic-Boreal region ranging from 44.2 to 47.1  $TgCH_4$   $y^{-1}$ , with wetland emissions being the main  $CH_4$  source  
 361 to the atmosphere. Depending on the parameter set in the prior flux setup by JSBACH, the annual mean wetland emission  
 362 ranges from 20.9 to 25.0  $TgCH_4$   $y^{-1}$  (47-54% of total emissions). The largest posterior wetland  $CH_4$  emissions were estimated  
 363 for western Russia (range of 6.9-8.4  $TgCH_4$   $y^{-1}$ , depending on the parameter set), followed by eastern Russia (range of 6.0-7.5  
 364  $TgCH_4$   $y^{-1}$ ), eastern Canada (range of 4.3-4.9  $TgCH_4$   $y^{-1}$ ), western Canada (range of 1.7-1.8  $TgCH_4$   $y^{-1}$ ), Alaska (range of 1.0-  
 365 2.0  $TgCH_4$   $y^{-1}$ ) and Europe including Greenland (range of 0.7-0.8  $TgCH_4$   $y^{-1}$ )  
 366

367 At the pan-Arctic scale, posterior wetland fluxes are higher than prior fluxes in the experiments using  $CH_4$  production  
 368  $Q_{10}$  values of 1.8 (8-22% higher than prior) and 2.2 (37-54% higher), see Table 1 and Fig. 3a. This suggests that these prior

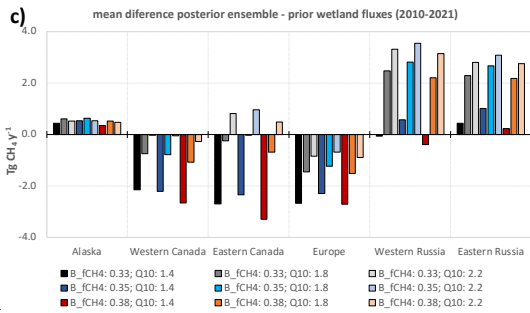
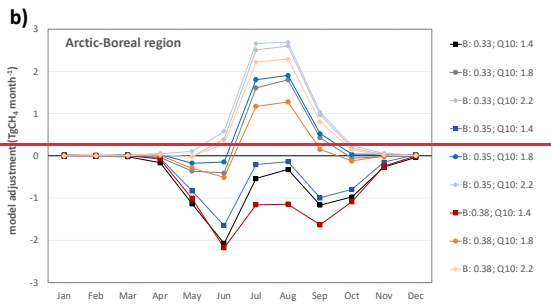
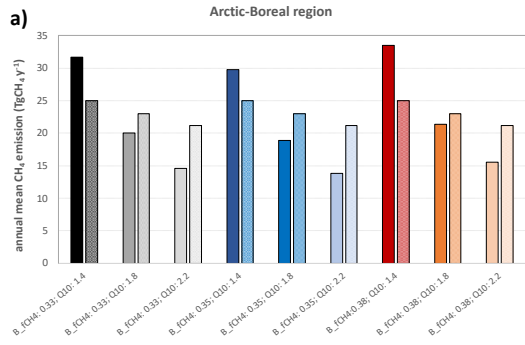
369 estimates underestimate CH<sub>4</sub> emissions in the Arctic–Boreal region relative to the observation-constrained posterior fluxes.  
370 However, prior fluxes estimated using a Q<sub>10</sub> value of 1.4 are higher than posterior fluxes (16-25% higher than posterior),  
371 indicating overestimation of CH<sub>4</sub> emissions in this case. When comparing the model adjustment for the three experiments  
372 (varying only the Q<sub>10</sub> parameters), the prior flux using Q<sub>10</sub> values of 1.8 produces the best agreement between prior and  
373 posterior flux budgets, meaning that a minimum adjustment in the inverse model optimization is required when considering  
374 annual mean emissions in the entire Arctic-Boreal region. Additionally, when comparing the different baseline  $f_{CH_4}$  fractions  
375 (using the Q<sub>10</sub> value with the best fit: 1.8), the minimum adjustment in the inverse model optimization is required for the prior  
376 flux with the largest baseline  $f_{CH_4}$  fraction (0.38), with posterior flux being 8% (2.0 TgCH<sub>4</sub> y<sup>-1</sup>) higher than the prior.

377 Our posterior estimates of CH<sub>4</sub> emissions from wetlands are similar to previous Arctic-Boreal estimates. Using a process-  
378 oriented ecosystem model, Christensen et al. (1996) estimated a total CH<sub>4</sub> emissions from northern wetlands and tundra (>  
379 50°N) to be 20 ± 13 TgCH<sub>4</sub> y<sup>-1</sup>. (Yuan et al. 2024) reported a mean annual emission of 20.3 ± 0.9 TgCH<sub>4</sub> y<sup>-1</sup> from boreal-Arctic  
380 wetland based on upscaled flux observations for the period 2002-2021. The Global Carbon Project estimated a mean annual  
381 wetland (including inland freshwaters) CH<sub>4</sub> emission for regions north of 60°N at 24 (9-53) TgCH<sub>4</sub> y<sup>-1</sup>, while top-down  
382 approaches resulted in a lower estimate of 9 (7-17) TgCH<sub>4</sub> y<sup>-1</sup> for the same region (Saunio et al., 2025). Recently, Ying et al.,  
383 (2025) estimated an annual mean CH<sub>4</sub> emissions from vegetated wetlands north of 45°N during 2016-2022 at  
384 22.8 ± 2.4 TgCH<sub>4</sub> y<sup>-1</sup>, ranging from 15.7 ± 1.8 TgCH<sub>4</sub> y<sup>-1</sup> to 51.6 ± 2.2 TgCH<sub>4</sub> y<sup>-1</sup>, depending on the wetland dataset used in the  
385 machine-learning-based upscaling approach. Although our posterior estimates are within the range of previous Arctic-Boreal  
386 estimates, direct comparisons are difficult because of differences in the study period, methodological approach, and  
387 inconsistent or unclear definitions of the spatial domain.

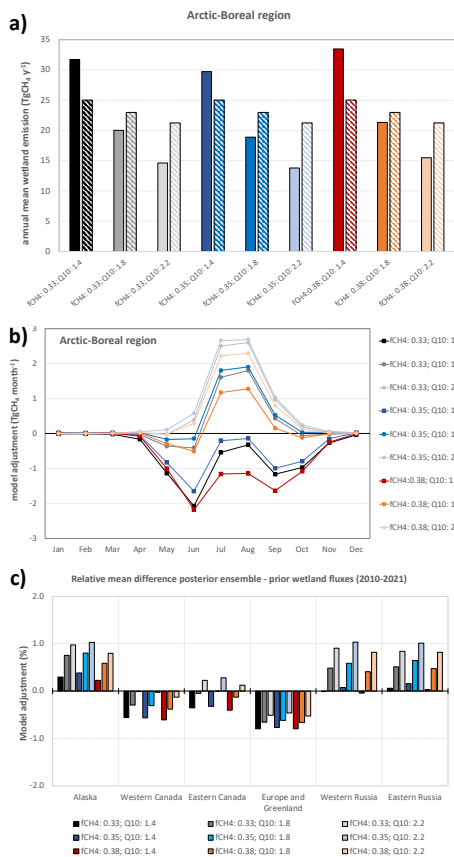
388

### 389 3.3 Seasonal variability in optimum CH<sub>4</sub> production Q<sub>10</sub> settings

390 Before analyzing regional differences in optimum CH<sub>4</sub> production Q<sub>10</sub> settings, we first focused on a clear seasonal  
391 pattern in the adjustments between prior and posterior CH<sub>4</sub> emissions, which showed a peak of changes occurring during  
392 summer. We therefore assessed whether the Q<sub>10</sub> value resulting in the minimum adjustment remained constant throughout the  
393 year or varied by season. At a pan-Arctic scale, seasonal variations were evident: estimates using CH<sub>4</sub> production Q<sub>10</sub> equaling  
394 1.8 aligned better with atmospheric observations in spring and fall but substantially underestimated summer emissions (Fig.  
395 3b). In contrast, estimates using a Q<sub>10</sub> of 1.4 best ~~agreed well~~ aligned with the atmospheric observation during summer, reducing  
396 the discrepancy between top-down and bottom-up estimates during the growing season, but strongly overestimating emissions  
397 in spring and fall (Fig. 3b). This pattern is primarily driven by wetlands in Russia. (Bergman et al., 2000) found temporal  
398 variation in Q<sub>10</sub> at peatland sites, suggesting that factors such as the availability of easily degradable compounds (e.g., root  
399 exudates) and the activity of anaerobic microbial biomass influence CH<sub>4</sub> production rates alongside temperature.



400



401 Figure 3. a) Annual mean CH<sub>4</sub> emissions (prior: full color bars; posterior: light-dashed color bars) for the entire Arctic-Boreal  
 402 region using all nine inversion scenarios with the different values of Q<sub>10</sub> parameter and baseline  $f_{CH_4}$  fraction in JSBACH  
 403 wetland emissions. b) adjustment of prior fluxes at monthly timesteps for the same model configurations as used in (a). c)  
 404 relative annual mean model adjustment as percentage of prior (posterior ensemble minus prior flux) for each one of the sub-  
 405 regions. Positive values indicate regions where prior estimates underestimated emissions compared with posterior estimates,  
 406 while negative values represent areas where prior emissions overestimate CH<sub>4</sub> emissions compared with the posterior  
 407 estimates.  
 408

### 409 3.4. Spatial patterns of best-fit model results based on posterior fluxes

411 CH<sub>4</sub> emissions exhibited spatial variability, and model adjustments were not uniform across the domain. This suggests  
 412 that the optimal parameterization varies by region and seasons (as discussed in Section 3.3). In some areas, Q<sub>10</sub> values of 1.4

Formatted: Indent: Left: 0 cm

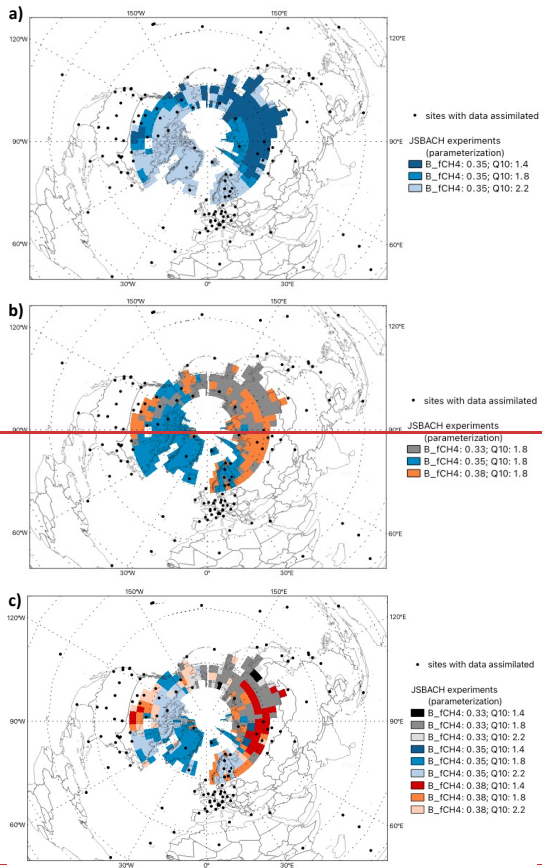
413 or 2.2 resulted in minimal adjustments (Fig. 3c), outperforming the model using a  $Q_{10}$  equaling 1.8 that was shown to work  
414 best as an average setting across the entire domain. To better evaluate this variability and explore ways to reduce uncertainty  
415 in specific regions, we assessed the best parameterization fit with observations at the per grid-cell level (Fig. 4).

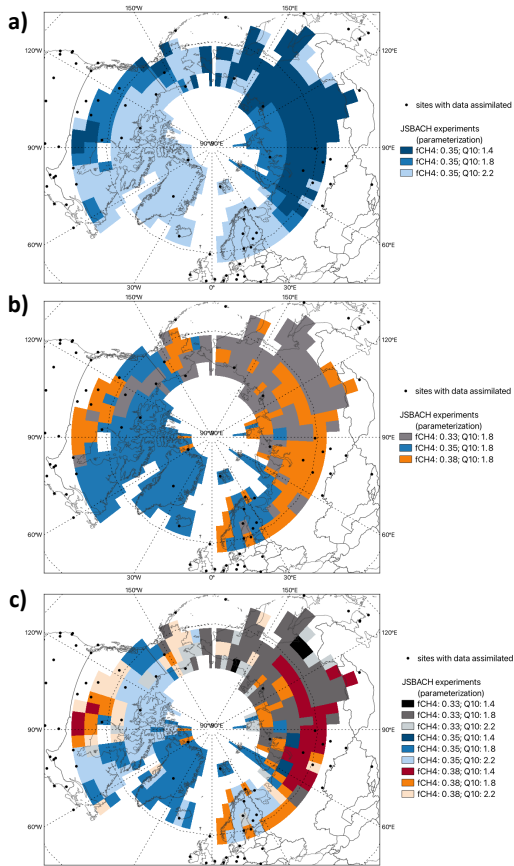
416 In our first analysis, we evaluated the spatial best fit model by keeping the baseline constant at a value of 0.35 and varying  
417 the  $CH_4$  production  $Q_{10}$  values (Fig. 4a). This spatial analysis showed that, in general, in regions with large wetland areas and  
418 high annual  $CH_4$  emissions (for example the Western Siberian Lowlands, [Supplementary Figures 1 and 2](#)) a  $Q_{10}$  value of 1.4  
419 resulted in the smallest model adjustment. As an increase in the  $Q_{10}$  parameter decreases  $CH_4$  production for temperatures  
420 below 295 K, a higher  $Q_{10}$  value in these regions results in an underestimation of emissions. In contrast, regions such as Europe  
421 and northern Canada showed, in general, minimum model adjustments with a  $Q_{10}$  value of 2.2, suggesting that lower  $Q_{10}$  value  
422 would overestimate wetland  $CH_4$  emissions in these regions. Interestingly, we observed adjustments with different signs in  
423 eastern Canada depending on the parameterization. For example, positive adjustments were associated with  $Q_{10}$  value of 2.2,  
424 as the prior emissions were underestimated compared with the estimated flux inferred from atmospheric observations.  
425 Additionally, we analyzed the effect of varying baseline flux values while keeping  $Q_{10}$  constant as 1.8, which showed that in  
426 high-emission areas, for example the Western Siberian Lowlands ([Supplementary Figures 1 and 2](#)), in general a larger baseline  
427 flux value led to the smallest model adjustments (Fig. 4b). When considering the model adjustment for all sensitivity tests  
428 (varying both  $CH_4$  production  $Q_{10}$  and baseline  $f_{CH_4}$  fraction) as shown in Fig. 4c, we also found a consistent pattern that  
429 confirmed the above findings varying only single parameters: the combination of higher baseline fluxes and lower  $Q_{10}$  value  
430 ( $Q_{10} = 1.4$ ) best captured  $CH_4$  dynamics in  $CH_4$  hotspots, as the Western Siberia Lowlands.

431 The wide range of reported incubation-based  $Q_{10}$  values for  $CH_4$  production in Arctic and northern wetlands depending  
432 on the site, substrate, and season, shows that the temperature sensitivity of  $CH_4$  production varies considerably across  
433 environments (Bergman et al., 2000; Roy Chowdhury et al., 2015; Treat et al., 2015). This variability, which could be driven  
434 by factors such as vegetation type, organic matter quality, and microbial activity, emphasizes the necessity of models to account  
435 for spatial differences in process rates. For example, one synthesis study reported a mean  $Q_{10}$  value of 1.18 for  $CH_4$  production  
436 under Arctic soil conditions (Roy Chowdhury et al., 2015; Treat et al., 2015). Roy Chowdhury et al. (2015) used anoxic  
437 laboratory incubations of active layer and permafrost samples from the Barrow Environmental Observatory in Alaska and  
438 reported a range of  $Q_{10}$  values from 1.8 to 22. Lupascu et al. (2012) reported that  $Q_{10}$  values describing the  $CH_4$  production  
439 response of peat to a 10 °C temperature change ranged from 1.9 to 3.5 in sedge sites and from 2.4 to 5.8 in *Sphagnum* mire  
440 sites, and suggested that using spatially variable  $CH_4$  production  $Q_{10}$  values could improve the accuracy of  $CH_4$  flux modeling  
441 in northern wetlands. Furthermore, Bergman et al. (2000) found that the seasonal average  $Q_{10}$  values ranged from  
442 approximately 4.6 to 9.2 depending on the plant community of the various peat types. Here, our intent is not to directly compare  
443 our results with reported incubation-based values, since our adjustments in the  $CH_4$  production  $Q_{10}$  refer to the  $Q_{10}$  of the  
444  $CH_4:CO_2$  production ratio, as represented in the model, and could not directly be comparable with  $CH_4$  production  $Q_{10}$  from  
445 the literature review. In JSBACH, the  $Q_{10}$  applied to  $CH_4$  production controls the fraction of  $CH_4$  generated, but the surface  
446 emission ratio may still be lower due to oxidation and transport pathways. Together, these examples highlight that  $CH_4$

447 production ~~are-is~~ strongly temperature dependent, and that the degree of this dependency can differ across regions and time  
448 periods. However, most current models cannot fully capture the influence of these factors due to structural limitations or a lack  
449 of detailed input data that is both spatially and temporally resolved. Consequently, these environmental drivers are often  
450 oversimplified or overlooked. Adjusting the CH<sub>4</sub> production Q<sub>10</sub> values, as we do here, offers a useful initial approach, but it  
451 should not be seen as a long-term solution. Ideally, future model and data developments will enable CH<sub>4</sub> production Q<sub>10</sub> values  
452 to adjust dynamically in response to underlying biophysical conditions, such as shifts in vegetation or organic matter  
453 characteristics. This will allow models to operate with a more generalizable formulation that still captures observed  
454 heterogeneity. Recent studies have demonstrated the potential of methane data assimilation techniques to optimize process-  
455 model parameters using observational constraints (Bernard et al., 2025; Monteil et al., 2025); however, regional and seasonal  
456 optimization remains largely unexplored. While ~~Although~~ our model experiments identified a single CH<sub>4</sub> production Q<sub>10</sub> value  
457 that best agrees with observations at the pan-Arctic scale, they also showed that CH<sub>4</sub> emissions and model adjustments vary  
458 regionally. Some areas showed a substantial response to different Q<sub>10</sub> values, which further demonstrates that an approach  
459 using a single parameter value is not sufficient. This highlights the need for future data assimilation frameworks that allow for  
460 regional, and potentially seasonal, parameter optimization.

461  
462





464

465 Figure 4. Map of the prior flux setting leading to minimum model adjustment (posterior ensemble minus prior fluxes) for the  
 466 annual mean fluxes at each grid-cell for the Arctic-Boreal region varying the (a) CH<sub>4</sub> production Q<sub>10</sub> parameter only, (b)  
 467 baseline  $f_{CH_4}$  fraction only and (c) both Q<sub>10</sub> parameter and baseline  $f_{CH_4}$  fraction. As mentioned in Section 3.2, the configuration  
 468 with Q<sub>10</sub> = 1.8 and  $f_{CH_4}$  = 0.38 provides the best fit at the pan-Arctic scale. However, regional results show that this  
 469 configuration does not minimize flux adjustments everywhere.

470

### 471 3.5. Limitations of Top-Down CH<sub>4</sub> estimates

472 Our analysis shows that atmospheric inverse modeling is a useful tool for evaluating and guiding process-model  
 473 parameterizations when estimating wetland CH<sub>4</sub> emissions. However, it is important to note the limitations of the top-down

474 approach, especially its relatively coarse spatial resolution. Global inversions usually operate at spatial scales larger than the  
475 process models, limiting their ability to resolve fine-scale heterogeneity, local emission hotspots, and small-scale processes.  
476 Consequently, grid-cell-level emission estimates represent aggregated signals and cannot fully capture localized variability.  
477 Additionally, top-down estimates rely heavily on the spatial and temporal distribution of atmospheric observations  
478 assimilated into the model. Regions with sparse coverage, such as central and eastern Russia, can limit the ability to accurately  
479 identify emission sources and increase dependence on prior estimates. Furthermore, most surface observation sites at high  
480 latitudes only started providing measurements in the early 2010s. This limits the ability to assess multi-decadal changes in CH<sub>4</sub>  
481 emissions (Vogt et al., 2025).  
482 At the grid-cell scale, assimilating only atmospheric CH<sub>4</sub> observations reflect the combined influence of all sources and  
483 sinks, making it difficult to distinguish overlapping source sectors. However, differences in the spatial patterns and seasonality  
484 of emissions can be constrained by atmospheric CH<sub>4</sub> observations in inversions that solve for different source categories  
485 (Saunois et al., 2025). Furthermore, errors in atmospheric transport model can propagate into emission estimates (Houweling  
486 et al., 2017; Locatelli et al., 2013; Schuh et al., 2019). Despite these limitations, our approach demonstrated a strong potential  
487 to help reduce the discrepancy between bottom-up and top-down estimates, therefore improving the accuracy of wetland CH<sub>4</sub>  
488 emission estimates.

#### 489 4. Conclusions

490 Overall, our parameter sensitivity tests of bottom-up wetland emissions indicate that CH<sub>4</sub> production Q<sub>10</sub> has a stronger  
491 effect on emission variability than the baseline  $f_{CH_4}$  fraction. Our bottom-up estimates showed that increasing CH<sub>4</sub> production  
492 Q<sub>10</sub> from 1.4 to 2.2 decreased the annual mean wetland CH<sub>4</sub> emission in the Arctic–Boreal region by half. In addition, our  
493 analysis shows that a single Q<sub>10</sub> value cannot capture the complexity of CH<sub>4</sub> emission dynamics across the Arctic-Boreal  
494 region. CH<sub>4</sub> production Q<sub>10</sub> values of 1.8 and 2.2 underestimate hotspot emissions, mainly during summer. In contrast, a Q<sub>10</sub>  
495 value of 1.4 overestimates emissions in regions with lower annual mean wetland emissions, such as e.g., Europe and northern  
496 Canada. Furthermore, a baseline  $f_{CH_4}$  fraction value of 0.38 led to the smallest model adjustments in CH<sub>4</sub> hotspots. These  
497 findings emphasize the importance of selecting appropriate parameterizations to accurately represent wetland emissions,  
498 especially in regions with substantial CH<sub>4</sub> release. Future models should incorporate dynamic, data-driven adjustments to  
499 reflect underlying environmental controls more accurately. If a varying CH<sub>4</sub> production Q<sub>10</sub> value approach is not feasible for  
500 this region due to computational cost or model setup constraints, using a Q<sub>10</sub> value of 1.8 provides the more similar CH<sub>4</sub>  
501 emission estimates compared to the atmospheric data across the entire Arctic-Boreal region.

502 Our results demonstrate that, despite the inherent limitations of top-down approaches when it comes to resolving fine scale  
503 heterogeneity, combining atmospheric inversions and process-models provides an important tool for reconciling discrepancies  
504 between bottom-up and top-down estimates, thereby improving constraints on large-scale wetland methane emissions.

505 Guidance by atmospheric inversion could therefore be instrumental to ensure the regional representativeness, and where  
506 applicable temporal variability, of process model parameter settings.

507 Our analysis shows that atmospheric inverse modeling is a useful tool for evaluating and guiding process model  
508 parameterizations when estimating wetland CH<sub>4</sub> emissions. However, it is important to note the limitations of the top-down  
509 approach. Top-down estimates rely heavily on the spatial and temporal distribution of atmospheric observations incorporated  
510 into the model. Regions with limited data or gaps, such as eastern Russia, can limit the ability to accurately identify emission  
511 sources and increase dependence on prior estimates. Global atmospheric inversions often operate at coarser spatial resolutions  
512 than the process models, and emission variability, including hotspot emissions, reducing the ability to estimate local scale  
513 process. At the grid-cell scale, assimilating only atmospheric CH<sub>4</sub> observations that is a result of total emissions (the balance  
514 between all sources and sinks) does not differentiate the overlapping source sectors in a grid-cell. However, differences in the  
515 spatial patterns and seasonality of emissions can be constrained by atmospheric CH<sub>4</sub> observations in inversions that solve for  
516 different sources categories. Furthermore, errors in atmospheric transport model can propagate into emission estimates.  
517 Despite these limitations, our approach demonstrated a strong potential to help reduce the discrepancy between bottom-up and  
518 top-down estimates, therefore improving the accuracy of wetland CH<sub>4</sub> emission estimates.

## 519 5. Authors contributions

520 LSB, MG, GG, VB designed the methodology. LSB wrote the first version of the manuscript and performed analysis and CH<sub>4</sub>  
521 inversions. GG performed and provided the JSBACH simulations. CR provided guidance and technical support for the inverse  
522 modelling. CB provided additional input on the discussion of results. All authors contributed with analysis and text. MG  
523 supervised and acquired funding.

## 524 6. Data and code availability

525 The prior and posterior mean Arctic-Boreal CH<sub>4</sub> fluxes on the CarboScope model horizontal resolution will be available in a  
526 data repository if the paper is accepted for publication. Observations from the NOAA GML network can be downloaded from  
527 the dedicated Observation Package (ObsPack) web server at <http://doi.org/10.25925/20231001>. The dataset “European  
528 atmospheric CO<sub>2</sub>, CH<sub>4</sub> and N<sub>2</sub>O Mole Fraction data product – 2024” analyzed during the current study was downloaded from  
529 the ICOS Carbon portal, DOI: <https://doi.org/10.18160/KDMT-V6CG>. The observations from the WDCGG dataset are  
530 available at [https://doi.org/10.50849/WDCGG\\_CH4\\_ALL\\_2023](https://doi.org/10.50849/WDCGG_CH4_ALL_2023). ATTO tower data can be request at  
531 <https://www.attodata.org/>. Observations from the Japan-Russia Siberian Tall Tower Inland Observation Network (JR-  
532 STATION) (Sasakawa et al., 2010) can be downloaded from <https://doi.org/10.17595/20231117.001>,  
533 <https://doi.org/10.17595/20231117.002>, <https://doi.org/10.17595/20231117.004>, <https://doi.org/10.17595/20231117.005>,

534 <https://doi.org/10.17595/20231117.006>, <https://doi.org/10.17595/20231117.007>, <https://doi.org/10.17595/20231117.008>. CH<sub>4</sub>  
535 [observations from the western Taimyr Peninsula \(Siberia\) can be downloaded from http://doi.org/10.17632/get3dddrh.1.](http://doi.org/10.17632/get3dddrh.1)

#### 536 **6-7. Competing interests**

537 The authors declare that they have no conflict of interest.

#### 538 **7-8. Acknowledgements**

539 The authors were funded by the European Research Council (ERC synergy project Q-Arctic, grant agreement no. 951288), the  
540 German Federal Ministry of Research, Technology and Space (MOMENT project, support code 03F0931G), and the AMPAC-  
541 net initiative (European Space Agency, grant no. 4000137912/22/I-DT). [The authors would also like to thank Dr. Santiago](#)  
542 [Botía at MPI-BGC/BSI for his valuable comments and suggestions, which helped us to improve this manuscript. The authors](#)  
543 [would like to acknowledge the contributions of Tonatiuh Nunez Ramirez, who designed the CH<sub>4</sub> chemistry model for](#)  
544 [CarboScope inversion system used in this work.](#)  
545 [We would like to thank all Principal Investigators and supporting staff for setting up and maintaining observation sites around](#)  
546 [the world, particularly in the Arctic, and for making the data available through different databases, including NOAA Obspack,](#)  
547 [ICOS RI, WDCGG and JR-STATION. The ICOS activities at Ricerca sul Sistema Energetico \(PRS\) station are financed by](#)  
548 [the Research Fund for the Italian Electrical System under the Three-Year Research Plan 2025-2027 \(MASE, Decree n.388 of](#)  
549 [November 6th, 2024\), in compliance with the Decree of April 12th, 2024. Although not fundamental to our study, we use](#)  
550 [ATTO methane data from 2012 to 2019 and for this we want to acknowledge Jost Lavric and the ATTO consortium for making](#)  
551 [the data available. This work is based on use of Large Research Infrastructure CzeCOS supported by the Ministry of Education,](#)  
552 [Youth and Sports of CR within the CzeCOS program, grant number LM2023048.](#)  
553 [Parts of the text was language-edited for grammatical correctness using DeepL. The authors have reviewed and verified the](#)  
554 [content as needed and take full responsibility for it.](#)~~We would like to thank all Principal Investigators and supporting staff for~~  
555 ~~setting up and maintaining observation sites around the world, particularly in the Arctic, and for making the data available~~  
556 ~~through different databases. The authors would also like to thank Santiago Botía at MPI-BGC/BSI for his valuable comments~~  
557 ~~and suggestions, which helped us to improve this manuscript. The authors would like to acknowledge the contributions of~~  
558 ~~Tonatiuh Nunez Ramirez, who designed the CH<sub>4</sub> chemistry model for CarboScope inversion system used in this work. Parts~~  
559 ~~of the text was language-edited for grammatical correctness using DeepL. The authors have reviewed and verified the content~~  
560 ~~as needed and take full responsibility for it.~~

561 **8-9. References**

- 562 Bergman, I., Klarqvist, M., and Nilsson, M.: Seasonal variation in rates of methane production from peat of various botanical  
563 origins: effects of temperature and substrate quality, *FEMS Microbiol. Ecol.*, 33, 181–189, <https://doi.org/10.1111/j.1574-6941.2000.tb00740.x>, 2000.
- 564
- 565 Bernard, J., Salmon, E., Saunois, M., Peng, S., Serrano-Ortiz, P., Berchet, A., Gnanamoorthy, P., Jansen, J., and Ciais, P.:  
566 Satellite-based modeling of wetland methane emissions on a global scale (SatWetCH4 1.0), *Geosci. Model Dev.*, 18, 863–883,  
567 <https://doi.org/10.5194/gmd-18-863-2025>, 2025.
- 568 BEVEN, K. J. and KIRKBY, M. J.: A physically based, variable contributing area model of basin hydrology / Un modèle à  
569 base physique de zone d'appel variable de l'hydrologie du bassin versant, *Hydrological Sciences Bulletin*, 24, 43–69,  
570 <https://doi.org/10.1080/02626667909491834>, 1979.
- 571 Chinta, S., Gao, X., and Zhu, Q.: Machine Learning Driven Sensitivity Analysis of E3SM Land Model Parameters for Wetland  
572 Methane Emissions, *J. Adv. Model. Earth Syst.*, 16, <https://doi.org/10.1029/2023MS004115>, 2024.
- 573 Christensen, T. R., Prentice, I. C., Kaplan, J., Haxeltine, A., and Sitch, S.: Methane flux from northern wetlands and tundra,  
574 *Tellus B: Chemical and Physical Meteorology*, 48, 652, <https://doi.org/10.3402/tellusb.v48i5.15938>, 1996.
- 575 Conrad, R.: Contribution of hydrogen to methane production and control of hydrogen concentrations in methanogenic soils  
576 and sediments, *FEMS Microbiol. Ecol.*, 28, 193–202, <https://doi.org/10.1111/j.1574-6941.1999.tb00575.x>, 1999.
- 577 Crippa, M., Guizzardi, D., Pagani, F., Banja, M., Muntean, M., Schaaf E., Becker, W., Monforti-Ferrario, F., Quadrelli, R.,  
578 Risquez Martin, A., Taghavi-Moharamli, P., Köykkä, J., Grassi, G., Rossi, S., Brandao De Melo, J., Oom, D., Branco, A., San-  
579 Miguel, J., and Vignati, E.: GHG emissions of all world countries, Luxembourg,  
580 <https://doi.org/https://data.europa.eu/doi/10.2760/953322>, 2023.
- 581 Ekici, A., Beer, C., Hagemann, S., Boike, J., Langer, M., and Hauck, C.: Simulating high-latitude permafrost regions by the  
582 JSBACH terrestrial ecosystem model, *Geosci. Model Dev.*, 7, 631–647, <https://doi.org/10.5194/gmd-7-631-2014>, 2014.
- 583 Etiope, G., Ciotoli, G., Schwietzke, S., and Schoell, M.: Gridded maps of geological methane emissions and their isotopic  
584 signature, *Earth Syst. Sci. Data*, 11, 1–22, <https://doi.org/10.5194/essd-11-1-2019>, 2019.
- 585 Goll, D. S., Brovkin, V., Liski, J., Raddatz, T., Thum, T., and Todd-Brown, K. E. O.: Strong dependence of CO<sub>2</sub> emissions  
586 from anthropogenic land cover change on initial land cover and soil carbon parametrization, *Global Biogeochem. Cycles*, 29,  
587 1511–1523, <https://doi.org/10.1002/2014GB004988>, 2015.
- 588 Guimberteau, M., Zhu, D., Maignan, F., Huang, Y., Yue, C., Dantec-Nédélec, S., Otlé, C., Jorner-Puig, A., Bastos, A., Laurent,  
589 P., Goll, D., Bowring, S., Chang, J., Guenet, B., Tifafi, M., Peng, S., Krinner, G., Ducharne, A., Wang, F., Wang, T., Wang,  
590 X., Wang, Y., Yin, Z., Lauerwald, R., Joetzier, E., Qiu, C., Kim, H., and Ciais, P.: ORCHIDEE-MICT (v8.4.1), a land surface  
591 model for the high latitudes: model description and validation, *Geosci. Model Dev.*, 11, 121–163, <https://doi.org/10.5194/gmd-11-121-2018>, 2018.

593 Hagemann, S. and Stacke, T.: Impact of the soil hydrology scheme on simulated soil moisture memory, *Clim. Dyn.*, **44**, 1731–  
594 1750, <https://doi.org/10.1007/s00382-014-2221-6>, 2015.

595 Harris, I. C.: CRUJRA: Collection of CRUJRA forcing datasets of gridded land surface blend of Climatic Research Unit (CRU)  
596 and Japanese reanalysis (JRA) data. Centre for Environmental Data Analysis, University of East Anglia Climatic Research  
597 Unit., 2019.

598 Heimann, M. and Körner, S.: The global atmospheric tracer model TM3: model description and user's manual release 3.8a,  
599 Jena, 2003.

600 Hossaini, R., Chipperfield, M. P., Saiz-Lopez, A., Fernandez, R., Monks, S., Feng, W., Brauer, P., and Glasow, R. von: A  
601 global model of tropospheric chlorine chemistry: Organic versus inorganic sources and impact on methane oxidation, *Journal*  
602 *of Geophysical Research: Atmospheres*, **121**, 14,271-14,297, <https://doi.org/10.1002/2016JD025756>, 2016.

603 Houweling, S., Bergamaschi, P., Chevallier, F., Heimann, M., Kaminski, T., Krol, M., Michalak, A. M., and Patra, P.: Global  
604 inverse modeling of CH<sub>4</sub> sources and sinks: an overview of methods, *Atmos. Chem. Phys.*, **17**, 235–256,  
605 <https://doi.org/10.5194/acp-17-235-2017>, 2017.

606 Hugelius, G., Ramage, J., Burke, E., Chatterjee, A., Smallman, T. L., Aalto, T., Bastos, A., Biasi, C., Canadell, J. G., Chandra,  
607 N., Chevallier, F., Ciais, P., Chang, J., Feng, L., Jones, M. W., Kleinen, T., Kuhn, M., Lauerwald, R., Liu, J., López-Blanco,  
608 E., Luijkx, I. T., Marushchak, M. E., Natali, S. M., Niwa, Y., Olefeldt, D., Palmer, P. I., Patra, P. K., Peters, W., Potter, S.,  
609 Poulter, B., Rogers, B. M., Riley, W. J., Saunio, M., Schuur, E. A. G., Thompson, R. L., Treat, C., Tsuruta, A., Turetsky, M.  
610 R., Virkkala, A. -M., Voigt, C., Watts, J., Zhu, Q., and Zheng, B.: Permafrost Region Greenhouse Gas Budgets Suggest a  
611 Weak CO<sub>2</sub> Sink and CH<sub>4</sub> and N<sub>2</sub>O Sources, But Magnitudes Differ Between Top-Down and Bottom-Up Methods, *Global*  
612 *Biogeochem. Cycles*, **38**, <https://doi.org/10.1029/2023GB007969>, 2024.

613 ICOS RI, Bergamaschi, P., Colomb, A., De Mazière, M., Emmenegger, L., Kubistin, D., Lehner, I., Lehtinen, K., Lund Myhre,  
614 C., Marek, M., O'Doherty, S., Platt, S. M., Plaß-Dülmer, C., Ramonet, M., Apadula, F., Arnold, S., Blanc, P.-E., Brunner, D.,  
615 Chen, H., Chmura, L., Conil, S., Couret, C., Cristofanelli, P., Delmotte, M., Forster, G., Frumau, A., Gheusi, F., Hammer, S.,  
616 Haszpra, L., Hatakka, J., Heliasz, M., Henne, S., Hoheisel, A., Kneuer, T., Laurila, T., Leskinen, A., Leuenberger, M., Levin,  
617 I., Lindauer, M., Lunder, C., Mammarella, I., Manca, G., Manning, A., Martin, D., Meinhardt, F., Mölder, M., Müller-  
618 Williams, J., Necki, J., Ottosson-Löfvenius, M., Philippon, C., Piacentino, S., Pitt, J., Rivas-Soriano, P., Scheeren, B.,  
619 Schumacher, M., Sha, M. K., Smith, P., Spain, G., Steinbacher, M., Sørensen, L. L., Vermeulen, A., Vítková, G., Xueref-  
620 Remy, I., di Sarra, A., Conen, F., Kazan, V., Roulet, Y.-A., Biermann, T., Heltai, D., D.Hensen, A., Hermansen, O.,  
621 Komínková, K., Laurent, O., Levula, J., Lopez, M., Marklund, P., Pichon, J.-M., Schmidt, M., Stanley, K., and Trisolino, P.:  
622 European Obspack compilation of atmospheric methane data from ICOS and non-ICOS European stations for the period 1984-  
623 2024; *obspace\_ch4\_466\_GVeu\_2024-02-01*, <https://doi.org/https://doi.org/10.18160/KDMT-V6CG>, 2024.

624 Jöckel, P., Tost, H., Pozzer, A., Brühl, C., Buchholz, J., Ganzeveld, L., Hoor, P., Kerkweg, A., Lawrence, M. G., Sander, R.,  
625 Steil, B., Stiller, G., Tanarhte, M., Taraborrelli, D., van Aardenne, J., and Lelieveld, J.: The atmospheric chemistry general

626 circulation model ECHAM5/MESy1: consistent simulation of ozone from the surface to the mesosphere, *Atmos. Chem.*  
627 *Phys.*, 6, 5067–5104, <https://doi.org/10.5194/acp-6-5067-2006>, 2006.

628 Kalnay, E., Kanamitsu, M., Kistler, R., Collins, W., Deaven, D., Gandin, L., Iredell, M., Saha, S., White, G., Woollen, J., Zhu,  
629 Y., Leetmaa, A., Reynolds, R., Chelliah, M., Ebisuzaki, W., Higgins, W., Janowiak, J., Mo, K. C., Ropelewski, C., Wang, J.,  
630 Jenne, R., and Joseph, D.: The NCEP/NCAR 40-Year Reanalysis Project, *Bull. Am. Meteorol. Soc.*, 77, 437–471,  
631 [https://doi.org/10.1175/1520-0477\(1996\)077<0437:TNYRP>2.0.CO;2](https://doi.org/10.1175/1520-0477(1996)077<0437:TNYRP>2.0.CO;2), 1996.

632 Kim, H.-S., Maksyutov, S., Glagolev, M. V., Machida, T., Patra, P. K., Sudo, K., and Inoue, G.: Evaluation of methane  
633 emissions from West Siberian wetlands based on inverse modeling, *Environmental Research Letters*, 6, 035201,  
634 <https://doi.org/10.1088/1748-9326/6/3/035201>, 2011.

635 Kleinen, T., Mikolajewicz, U., and Brovkin, V.: Terrestrial methane emissions from the Last Glacial Maximum to the  
636 preindustrial period, *Climate of the Past*, 16, 575–595, <https://doi.org/10.5194/cp-16-575-2020>, 2020.

637 Knoblauch, C., Beer, C., Liebner, S., Grigoriev, M. N., and Pfeiffer, E.-M.: Methane production as key to the greenhouse gas  
638 budget of thawing permafrost, *Nat. Clim. Chang.*, 8, 309–312, <https://doi.org/10.1038/s41558-018-0095-z>, 2018.

639 Locatelli, R., Bousquet, P., Chevallier, F., Fortems-Cheney, A., Szopa, S., Saunio, M., Agusti-Panareda, A., Bergmann, D.,  
640 Bian, H., Cameron-Smith, P., Chipperfield, M. P., Gloor, E., Houweling, S., Kawa, S. R., Krol, M., Patra, P. K., Prinn, R. G.,  
641 Rigby, M., Saito, R., and Wilson, C.: Impact of transport model errors on the global and regional methane emissions estimated  
642 by inverse modelling, *Atmos. Chem. Phys.*, 13, 9917–9937, <https://doi.org/10.5194/acp-13-9917-2013>, 2013.

643 Lupascu, M., Wadham, J. L., Hornibrook, E. R. C., and Pancost, R. D.: Temperature Sensitivity of Methane Production in the  
644 Permafrost Active Layer at Stordalen, Sweden: A Comparison with Non-permafrost Northern Wetlands, *Arct. Antarct. Alp.*  
645 *Res.*, 44, 469–482, <https://doi.org/10.1657/1938-4246-44.4.469>, 2012.

646 Mauritsen, T., Bader, J., Becker, T., Behrens, J., Bittner, M., Brokopf, R., Brovkin, V., Claussen, M., Crueger, T., Esch, M.,  
647 Fast, I., Fiedler, S., Fläschner, D., Gayler, V., Giorgetta, M., Goll, D. S., Haak, H., Hagemann, S., Hedemann, C., Hohenegger,  
648 C., Ilyina, T., Jahns, T., Jimenéz-de-la-Cuesta, D., Jungclaus, J., Kleinen, T., Kloster, S., Kracher, D., Kinne, S., Kleberg, D.,  
649 Lasslop, G., Kornbluh, L., Marotzke, J., Matei, D., Meraner, K., Mikolajewicz, U., Modali, K., Möbis, B., Müller, W. A.,  
650 Nabel, J. E. M. S., Nam, C. C. W., Notz, D., Nyawira, S., Paulsen, H., Peters, K., Pincus, R., Pohlmann, H., Pongratz, J., Popp,  
651 M., Raddatz, T. J., Rast, S., Redler, R., Reick, C. H., Rohrschneider, T., Schemann, V., Schmidt, H., Schnur, R., Schulzweida,  
652 U., Six, K. D., Stein, L., Stemmler, I., Stevens, B., von Storch, J., Tian, F., Voigt, A., Vrese, P., Wieners, K., Wilkenskeld,  
653 S., Winkler, A., and Roeckner, E.: Developments in the MPI-M Earth System Model version 1.2 (MPI-ESM1.2) and Its  
654 Response to Increasing CO<sub>2</sub>, *J. Adv. Model. Earth Syst.*, 11, 998–1038, <https://doi.org/10.1029/2018MS001400>, 2019.

655 Miller, S. M., Commane, R., Melton, J. R., Andrews, A. E., Benmergui, J., Dlugokencky, E. J., Janssens-Maenhout, G.,  
656 Michalak, A. M., Sweeney, C., and Worthy, D. E. J.: Evaluation of wetland methane emissions across North America using  
657 atmospheric data and inverse modeling, *Biogeosciences*, 13, 1329–1339, <https://doi.org/10.5194/bg-13-1329-2016>, 2016.

658 Monteil, G., Theanutti Kallingal, J., and Scholze, M.: CH<sub>4</sub> emissions from Northern Europe wetlands: compared data  
659 assimilation approaches, *Atmos. Chem. Phys.*, 25, 14251–14277, <https://doi.org/10.5194/acp-25-14251-2025>, 2025.

660 Moser, M., Kaiser, L., Brovkin, V., and Beer, C.: Reviews and syntheses: The role of process-based modeling of the CO<sub>2</sub> : CH  
661<sub>4</sub> production ratio in predicting future terrestrial Arctic methane emissions, *Biogeosciences*, 23, 605–621,  
662 <https://doi.org/10.5194/bg-23-605-2026>, 2026.

663 Olefeldt, D., Hovemyr, M., Kuhn, M. A., Bastviken, D., Bohn, T. J., Connolly, J., Crill, P., Euskirchen, E. S., Finkelstein, S.  
664 A., Genet, H., Grosse, G., Harris, L. I., Heffernan, L., Helbig, M., Hugelius, G., Hutchins, R., Juutinen, S., Lara, M. J.,  
665 Malhotra, A., Manies, K., McGuire, A. D., Natali, S. M., O'Donnell, J. A., Parmentier, F.-J. W., Räsänen, A., Schädel, C.,  
666 Sonnentag, O., Strack, M., Tank, S. E., Treat, C., Varner, R. K., Virtanen, T., Warren, R. K., and Watts, J. D.: The Boreal–  
667 Arctic Wetland and Lake Dataset (BAWLD), *Earth Syst. Sci. Data*, 13, 5127–5149, [https://doi.org/10.5194/essd-13-5127-](https://doi.org/10.5194/essd-13-5127-2021)  
668 2021, 2021.

669 Panov, A., Prokushkin, A., Kübler, K. R., Korets, M., Urban, A., Bondar, M., and Heimann, M.: Continuous CO<sub>2</sub> and CH<sub>4</sub>  
670 Observations in the Coastal Arctic Atmosphere of the Western Taimyr Peninsula, Siberia: The First Results from a New  
671 Measurement Station in Dikson, *Atmosphere (Basel)*, 12, 876, <https://doi.org/10.3390/atmos12070876>, 2021.

672 Poulter, B., Bousquet, P., Canadell, J. G., Ciais, P., Peregon, A., Saunio, M., Arora, V. K., Beerling, D. J., Brovkin, V., Jones,  
673 C. D., Joos, F., Gedney, N., Ito, A., Kleinen, T., Koven, C. D., McDonald, K., Melton, J. R., Peng, C., Peng, S., Prigent, C.,  
674 Schroeder, R., Riley, W. J., Saito, M., Spahni, R., Tian, H., Taylor, L., Viovy, N., Wilton, D., Wiltshire, A., Xu, X., Zhang,  
675 B., Zhang, Z., and Zhu, Q.: Global wetland contribution to 2000–2012 atmospheric methane growth rate dynamics,  
676 *Environmental Research Letters*, 12, 094013, <https://doi.org/10.1088/1748-9326/aa8391>, 2017.

677 Rantanen, M., Karpechko, A. Yu., Lipponen, A., Nordling, K., Hyvärinen, O., Ruosteenoja, K., Vihma, T., and Laaksonen,  
678 A.: The Arctic has warmed nearly four times faster than the globe since 1979, *Commun. Earth Environ.*, 3, 168,  
679 <https://doi.org/10.1038/s43247-022-00498-3>, 2022.

680 Reick, C. H., Gayler, V., Goll, D., Hagemann, S., Heidkamp, M., Nabel, J. E. M. S., Raddatz, T., Roeckner, E., Schnur, R.,  
681 and Wilkenskjaeld, S.: JSBACH 3 - The land component of the MPI Earth System Model: documentation of version 3.2, 2021.

682 Ricciuto, D. M., Xu, X., Shi, X., Wang, Y., Song, X., Schadt, C. W., Griffiths, N. A., Mao, J., Warren, J. M., Thornton, P. E.,  
683 Chanton, J., Keller, J. K., Bridgman, S. D., Gutknecht, J., Sebestyen, S. D., Finzi, A., Kolka, R., and Hanson, P. J.: An  
684 Integrative Model for Soil Biogeochemistry and Methane Processes: I. Model Structure and Sensitivity Analysis, *J. Geophys.*  
685 *Res. Biogeosci.*, 126, <https://doi.org/10.1029/2019JG005468>, 2021.

686 Riley, W. J., Subin, Z. M., Lawrence, D. M., Swenson, S. C., Torn, M. S., Meng, L., Mahowald, N. M., and Hess, P.: Barriers  
687 to predicting changes in global terrestrial methane fluxes: analyses using CLM4Me, a methane biogeochemistry model  
688 integrated in CESM, *Biogeosciences*, 8, 1925–1953, <https://doi.org/10.5194/bg-8-1925-2011>, 2011.

689 Rödenbeck, C.: Estimating CO<sub>2</sub> sources and sinks from atmospheric mixing ratio measurements using a global inversion of  
690 atmospheric transport, Jena, 2005.

691 Roy Chowdhury, T., Herndon, E. M., Phelps, T. J., Elias, D. A., Gu, B., Liang, L., Wullschlegel, S. D., and Graham, D. E.:  
692 Stoichiometry and temperature sensitivity of methanogenesis and <math>\text{CO}\_2</math> production from saturated polygonal  
693 tundra in Barrow, Alaska, *Glob. Chang. Biol.*, 21, 722–737, <https://doi.org/10.1111/gcb.12762>, 2015.

694 Sasakawa, M., Shimoyama, K., Machida, T., Tsuda, N., Suto, H., Arshinov, M., Davydov, D., Fofonov, A., Krasnov, O., Saeki,  
695 T., Koyama, Y., and Maksyutov, S.: Continuous measurements of methane from a tower network over Siberia, *Tellus B:*  
696 *Chemical and Physical Meteorology*, 62, 403, <https://doi.org/10.1111/j.1600-0889.2010.00494.x>, 2010.

697 Sasakawa, M., Tsuda, N., Machida, T., Arshinov, M., Davydov, D., Fofonov, A., and Belan, B.: Revised methodology for CO  
698 <sub>2</sub> and CH<sub>4</sub> measurements at remote sites using a working standard-gas-saving system, *Atmos. Meas. Tech.*, 18, 1717–1730,  
699 <https://doi.org/10.5194/amt-18-1717-2025>, 2025.

700 Saunio, M., Martinez, A., Poulter, B., Zhang, Z., Raymond, P. A., Regnier, P., Canadell, J. G., Jackson, R. B., Patra, P. K.,  
701 Bousquet, P., Ciais, P., Dlugokencky, E. J., Lan, X., Allen, G. H., Bastviken, D., Beerling, D. J., Belikov, D. A., Blake, D. R.,  
702 Castaldi, S., Crippa, M., Deemer, B. R., Dennison, F., Etiope, G., Gedney, N., Höglund-Isaksson, L., Holgerson, M. A.,  
703 Hopcroft, P. O., Hugelius, G., Ito, A., Jain, A. K., Janardanan, R., Johnson, M. S., Kleinen, T., Krummel, P. B., Lauerwald,  
704 R., Li, T., Liu, X., McDonald, K. C., Melton, J. R., Mühle, J., Müller, J., Murguía-Flores, F., Niwa, Y., Noce, S., Pan, S.,  
705 Parker, R. J., Peng, C., Ramonet, M., Riley, W. J., Rocher-Ros, G., Rosentreter, J. A., Sasakawa, M., Segers, A., Smith, S. J.,  
706 Stanley, E. H., Thanwerdas, J., Tian, H., Tsuruta, A., Tubiello, F. N., Weber, T. S., van der Werf, G. R., Worthy, D. E. J., Xi,  
707 Y., Yoshida, Y., Zhang, W., Zheng, B., Zhu, Q., Zhu, Q., and Zhuang, Q.: Global Methane Budget 2000–2020, *Earth Syst.*  
708 *Sci. Data*, 17, 1873–1958, <https://doi.org/10.5194/essd-17-1873-2025>, 2025.

709 Schuh, A. E., Jacobson, A. R., Basu, S., Weir, B., Baker, D., Bowman, K., Chevallier, F., Crowell, S., Davis, K. J., Deng, F.,  
710 Denning, S., Feng, L., Jones, D., Liu, J., and Palmer, P. I.: Quantifying the Impact of Atmospheric Transport Uncertainty on  
711 CO<sub>2</sub> Surface Flux Estimates, *Global Biogeochem. Cycles*, 33, 484–500, <https://doi.org/10.1029/2018GB006086>, 2019.

712 Schuldt, K. N., Mund, J., Aalto, T., Andrews, A., Apadula, F., Jgor Arduini, Arnold, S., Baier, B., Bani, L., Bartyzel, J.,  
713 Bergamaschi, P., Biermann, T., Biraud, S. C., Pierre-Eric Blanc, Boenisch, H., Brailsford, G., Brand, W. A., Brunner, D., Bui,  
714 T. P. V., and Miroslaw Zimnoch: Multi-laboratory compilation of atmospheric carbon dioxide data for the period 1983-2022;  
715 *obspack\_ch4\_1\_GLOBALVIEWplus\_v6.0\_2023-12-01* [Data set]. NOAA Global Monitoring Laboratory.  
716 <http://doi.org/10.25925/20231001>, 2023.

717 Sellar, A. A., Jones, C. G., Mulcahy, J. P., Tang, Y., Yool, A., Wiltshire, A., O'Connor, F. M., Stringer, M., Hill, R., Palmieri,  
718 J., Woodward, S., de Mora, L., Kuhlbrodt, T., Rumbold, S. T., Kelley, D. I., Ellis, R., Johnson, C. E., Walton, J., Abraham, N.,  
719 L., Andrews, M. B., Andrews, T., Archibald, A. T., Berthou, S., Burke, E., Blockley, E., Carslaw, K., Dalvi, M., Edwards, J.,  
720 Folberth, G. A., Gedney, N., Griffiths, P. T., Harper, A. B., Hendry, M. A., Hewitt, A. J., Johnson, B., Jones, A., Jones, C. D.,  
721 Keeble, J., Liddicoat, S., Morgenstern, O., Parker, R. J., Predoi, V., Robertson, E., Siahhaan, A., Smith, R. S., Swaminathan,  
722 R., Woodhouse, M. T., Zeng, G., and Zerroukat, M.: UKESM1: Description and Evaluation of the U.K. Earth System Model,  
723 *J. Adv. Model. Earth Syst.*, 11, 4513–4558, <https://doi.org/10.1029/2019MS001739>, 2019.

724 Spahni, R., Wania, R., Neef, L., van Weele, M., Pison, I., Bousquet, P., Frankenberg, C., Foster, P. N., Joos, F., Prentice, I. C.,  
725 and van Velthoven, P.: Constraining global methane emissions and uptake by ecosystems, *Biogeosciences*, 8, 1643–1665,  
726 <https://doi.org/10.5194/bg-8-1643-2011>, 2011.

727 Spivakovsky, C. M., Logan, J. A., Montzka, S. A., Balkanski, Y. J., Foreman-Fowler, M., Jones, D. B. A., Horowitz, L. W.,  
728 Fusco, A. C., Brenninkmeijer, C. A. M., Prather, M. J., Wofsy, S. C., and McElroy, M. B.: Three-dimensional climatological  
729 distribution of tropospheric OH: Update and evaluation, *Journal of Geophysical Research: Atmospheres*, 105, 8931–8980,  
730 <https://doi.org/10.1029/1999JD901006>, 2000.

731 Treat, C. C., Natali, S. M., Ernakovich, J., Iversen, C. M., Lupascu, M., McGuire, A. D., Norby, R. J., Roy Chowdhury, T.,  
732 Richter, A., Šantrůčková, H., Schädel, C., Schuur, E. A. G., Sloan, V. L., Turetsky, M. R., and Waldrop, M. P.: A pan-Arctic  
733 synthesis of CH<sub>4</sub> and CO<sub>2</sub> production from anoxic soil incubations, *Glob. Chang. Biol.*, 21, 2787–2803,  
734 <https://doi.org/10.1111/gcb.12875>, 2015.

735 Tuomi, M., Rasinmäki, J., Repo, A., Vanhala, P., and Liski, J.: Soil carbon model Yasso07 graphical user interface,  
736 *Environmental Modelling & Software*, 26, 1358–1362, <https://doi.org/10.1016/j.envsoft.2011.05.009>, 2011.

737 Vogt, J., Pallandt, M. M. T. A., Basso, L. S., Bolek, A., Ivanova, K., Schlutow, M., Celis, G., Kuhn, M., Mauritz, M., Schuur,  
738 E. A. G., Arndt, K., Virkkala, A.-M., Wargowsky, I., and Göckede, M.: ARGO: ARctic greenhouse Gas Observation metadata  
739 version 1, *Earth Syst. Sci. Data*, 17, 2553–2573, <https://doi.org/10.5194/essd-17-2553-2025>, 2025.

740 Weber, T., Wiseman, N. A., and Kock, A.: Global ocean methane emissions dominated by shallow coastal waters, *Nat.*  
741 *Commun.*, 10, 4584, <https://doi.org/10.1038/s41467-019-12541-7>, 2019.

742 Ying, Q., Poulter, B., Watts, J. D., Arndt, K. A., Virkkala, A.-M., Bruhwiler, L., Oh, Y., Rogers, B. M., Natali, S. M., Sullivan,  
743 H., Armstrong, A., Ward, E. J., Schiferl, L. D., Elder, C. D., Peltola, O., Bartsch, A., Desai, A. R., Euskirchen, E., Göckede,  
744 M., Lehner, B., Nilsson, M. B., Peichl, M., Sonntag, O., Tuittila, E.-S., Sachs, T., Kalhori, A., Ueyama, M., and Zhang, Z.:  
745 WetCH<sub>4</sub>: a machine-learning-based upscaling of methane fluxes of northern wetlands during 2016–2022, *Earth Syst. Sci. Data*,  
746 17, 2507–2534, <https://doi.org/10.5194/essd-17-2507-2025>, 2025.

747 Yuan, K., Li, F., McNicol, G., Chen, M., Hoyt, A., Knox, S., Riley, W. J., Jackson, R., and Zhu, Q.: Boreal–Arctic wetland  
748 methane emissions modulated by warming and vegetation activity, *Nat. Clim. Chang.*, 14, 282–288,  
749 <https://doi.org/10.1038/s41558-024-01933-3>, 2024.

750 Zhang, Z., Poulter, B., Melton, J. R., Riley, W. J., Allen, G. H., Beerling, D. J., Bousquet, P., Canadell, J. G., Fluet-Chouinard,  
751 E., Ciais, P., Gedney, N., Hoperoff, P. O., Ito, A., Jackson, R. B., Jain, A. K., Jensen, K., Joos, F., Kleinen, T., Knox, S. H.,  
752 Li, T., Li, X., Liu, X., McDonald, K., McNicol, G., Miller, P. A., Müller, J., Patra, P. K., Peng, C., Peng, S., Qin, Z., Riggs, R.  
753 M., Saunio, M., Sun, Q., Tian, H., Xu, X., Yao, Y., Xi, Y., Zhang, W., Zhu, Q., Zhu, Q., and Zhuang, Q.: Ensemble estimates  
754 of global wetland methane emissions over 2000–2020, *Biogeosciences*, 22, 305–321, <https://doi.org/10.5194/bg-22-305-2025>,  
755 2025.

756  
757  
758  
759